InN-Based Heterojunction Field Effect Transistor

By

(Md. Sherajul Islam)

A thesis submitted in partial fulfillment of the requirements for the degree of
Master of Science in Electrical & Electronic Engineering

Khulna University of Engineering & Technology
Khulna 9203, Bangladesh

September 2009

Declaration

This is to certify that the thesis work entitled "***InN-Based Heterojunction Field Effect Transistor***" has been carried out by ***Md. Sherajul Islam*** in the Department of *Electrical & Electronic Engineering*, Khulna University of Engineering & Technology, Khulna-9203, Bangladesh. The above thesis work or any part of this work has not been submitted anywhere for the award of any degree or diploma.

12.09.2009

Signature of Supervisor

Signature of Student

Khulna University of Engineering & Technology
KUET
Bangladesh
Central Library

Approval

This is to certify that the thesis work submitted by Md. Sherajul Islam entitled ***"InN-Based Heterojunction Field Effect Transistor"*** has been approved by the board of examiners for the partial fulfillment of the requirements for the degree of M. Sc. Engineering in the Department of *Electrical & Electronic Engineering*, Khulna University of Engineering & Technology, Khulna-9203, Bangladesh in September 2009.

BOARD OF EXAMINERS

1. 12.09.09 — Chairman (Supervisor)
   Professor Dr. Ashraful G. Bhuiyan
   Dept. Electrical & Electronic Engineering
   Khulna University of Engineering & Technology

2. 12.09.09 — Member
   Professor Dr. Md. Rafiqul Islam
   Head, Dept. of Electrical & Electronic Engineering
   Khulna University of Engineering & Technology

3. 12/09/09 — Member
   Professor Dr. Nurunnabi Mollah
   Dept. of Electrical & Electronic Engineering
   Khulna University of Engineering & Technology

4. 120909 — Member
   Mr. A. N. M Enamul Kabir
   Associate Professor
   Dept. of Electrical & Electronic Engineering
   Khulna University of Engineering & Technology

5. 12.09.09 — Member (External)
   Professor Dr. Anisul Haque
   Chairperson, Dept. of Electrical & Electronic Engineering
   East West University, Dhaka, Bangladesh

ACKNOWLEDGEMENTS

First of all thanks to almighty ALLAH for successful completion of my thesis. I am indeed fortunate to have work under the guidance of **Prof. Dr. Ashraful G. Bhuiyan**. His contagious enthusiasm, originality and desired to succeed to have helped me complete into this thesis. His dedication to me and my work was instrumental in every successful endeavor of this research. Without doubt, completion of this work would not have been possible if not for his unwavering support through some very difficult times.

The reason I was able to finish this work was the close support from some persons. In particular, I would like to thank Md. Tanvir Hassan, Lecturer Dept of ETE, Daffodil International University, Mr. Sakib Muhammad Muhtadi and Md. Sazzad Hossain Students of 2k4 Batch for their valuable suggestions and other supports during this work.

I would like to thank Prof. Dr. Md. Rafiqul Islam, Head, Dept. of EEE. I feel proud having attended his classes on MOS Devices which made me interested in this field and encouraged me to do more advanced research work in future also.

I would grateful to Prof. Dr. Anisul Haque, Chairperson, Department of Electrical & Electronic Engineering, East West University, Dhaka, Bangladesh for his valuable suggestions during this work which helped me a lot.

Finally, I would like to thank all the faculty members of Electrical & Electronic Engineering Department for helping in various ways in formulating this dissertation.

I have to thank my family for being the ultimate source of strength and encouragement throughout my academic career and personal life. They have served as role models in various ways and I aspire to live up to their ideals. I hope this work in some way repays them for all of the love they have given me over the years.

Abstract

As a promising candidate for future high speed devices InN-based heterojunction field effect transistor (HFET) has gained a lot of attention in recent years. However, InN-based devices are still a less studied compared with other III-nitride based devices. This work describes a novel AlInN/InN heterojunction field effect transistor (HFET) without and with an oxide layer beneath the gate for high performance. A quantum mechanical charge control model based on the self-consistent solution of one dimensional Schrodinger-Poisson equations is developed. The transport properties such as channel mobility and the velocity-field characteristics of the proposed device are calculated using Monte Carlo simulation. In order to investigate dc and high frequency performances of the device an analytical drain current model is developed. The model takes into account the highly dominant spontaneous and piezoelectric polarization effects to predict the 2DEG sheet charge density more accurately at the heterointerface. The effect of parasitic source and drain resistances along with gate to source capacitance is incorporated in the high frequency analysis. The device transconductance is found from the channel current. The cut-off frequency is calculated using a simple equation relating transconductance and gate to source capacitance.

The investigated parameters of the proposed device are maximum drain current (I_{dmax}), threshold voltage (V_{th}), peak DC transconductance (g_m) and unity gain cut off frequency (f_t). The typical DC characteristics for a gate length of 0.25 μm with 100 μm gate width are as follows: I_{dmax} = 715 mA/mm, g_m = 280 mS/mm, f_t = 110 GHz and V_{th} = -2.50 V for HFET. While using an oxide layer of thickness 13 nm these values are: I_{dmax} = 786 mA/mm, g_m = 225 mS/mm, f_t = 154 GHz and V_{th} = - 2.52 V. The gate length dependence of transconductance and cut-off frequency in AlInN/InN HFET without and with an oxide layer has been theoretically investigated. In addition, the variation of these performance parameters with a gate to source voltage has also been studied. The calculated values of g_m is found to be varied from 280 to 205 mS/mm and 225 to 105

mS/mm for HFET without and with oxide layer, respectively with the variation of L_g from 0.25 to 1.5μm at V_{ds} = 2 and V_{gs} = 1.5V. The cut off frequency varies from 110 to 12 GHz and 154 to 26 GHz for HFET without and with oxide layer, respectively with the variation of L_g from 0.25 to 1.5 μm at V_{ds} = 2 V and V_{gs}= 1.5 V. The investigated results of the proposed device is compared with the GaN-based device and found to show excellent performance over the GaN-based devices.

The above studies indicate that the proposed InN-based HFET is very promising for the fabrication of high performance high speed devices.

Contents

		PAGE
Title Page		i
Declaration		ii
Approval		iii
Acknowledgement		iv
Abstract		v
Contents		vii
List of Tables		x
List of Figures		xi
Nomenclature		xiii
CHAPTER I	**Introduction**	1-5
	1.1 Overview	01
	1.2 Motivation and Objectives	03
	1.3 Outline of Dissertation	05
CHAPTER II	**Background Information**	6-16
	2.1 Introduction	06
	2.2 Polarization in III-Nitride materials	06
	2.3 Charge Control in an HFET	09
	2.4 Impact of polarization on sheet charge density	11
	2.5 AlInN/InN HFETs	12
	2.6 Issues Facing AlInN/InN HFETs	12
	2.7 Dielectric for InN MOSHFETs	13
	2.8 Modeling of FETs	15
	2.8.1 Empirical Models	15
	2.8.2 Table Based Models	16
	2.8.3 Physics Based Models	16

Khulna University of Engineering & Technology
KUET Bangladesh
Central Library

CHAPTER III	**Modeling of HFETs**	17-27
	3.1 Introduction	17
	3.2 Device Structure	17
	3.3 Charge Control Model	19
	3.4 Drain Current Model	22
	3.5 Transconductance Model	25
	3.6 Cut off frequency	26
CHAPTER IV	**Transport Properties**	28-38
	4.1 Introduction	28
	4.2 Charge Control Characteristics	
	4.2.1 Conduction Band Profile	28
	4.2.2 Position dependent charge distribution	30
	4.2.4 Composition dependent carrier concentration	31
	4.2.5 Variation of 2DEG Sheet Carrier Density with Gate to Source Voltage	32
	4.3 Scattering Mechanism	
	4.3.1 Mobility analysis	36
	4.3.2 Velocity field characteristics	37
CHAPTER V	**DC Characteristics Analysis**	39-45
	5.1 Introduction	39
	5.2 Threshold Voltage Characteristics	39
	5.3 I-V Characteristics	40
	5.4 Saturation Drain Current Characteristics	41
	5.5 Gate Length Dependent Drain Current	42
	5.6 Transconductance Variation with Gate to source Voltage	43
	5.7 Gate Length Dependent Transconductance	44
CHAPTER VI	**High Frequency Performance Analyses**	46-49
	6.1 Introduction	46
	6.2 Variation of Cut off Frequency with gate to source voltage	46

	6.3 Gate Length Dependent Cut off Frequency	48
	6.4 Cut off Frequency and Drain Current Relation	49
CHAPTER VII	**Conclusions and Recommendations**	50-53
	7.1 Conclusions	50
	7.2 Recommendations	52
References		54
Appendices		62

LIST OF TABLES

Table No	Description	Page
2.1	Spontaneous polarization, piezoelectric coefficients, elastic constants and c-plane lattice constants of InN, AlN and GaN	09
3.1	Parameters used in the DC and high frequency analysis	27

LIST OF FIGURES

Figure No	Description	Page
1.1	Velocity-field characteristics associated with wurtzite InN, GaN, AlN, and zinc blend GaAs.	03
2.1	Illustration of the convention used to determine polarity in wurtzitic nitride films	07
2.2	Polarization charge at the AlInN/InN interface	10
2.3	Cross section and corresponding band diagram of an HFET	11
3.1	Schematic view of the proposed InN based HFET	18
3.2	Conduction band profile of AlInN/InN based hetero Structure with an oxide layer beneath the gate along the y-axis	19
4.1	Simulated conduction band profile of AlInN/InN HFET	29
4.2	Simulated conduction band profile of AlInN/InN MOSHFET	29
4.3	Simulated electron distribution as a function of distance of AlInN/InN HFET	30
4.4	Simulated electron distribution as a function of distance of AlInN/InN MOSHFET	31
4.5	Electron peak concentration as a function of In content of AlInN/InN HFET	32
4.6	Variation of 2DEG sheet carrier density with gate source voltage for different In content	33
4.7	Variation of 2DEG sheet carrier density with gate source voltage for HFET and MOSHFET	33
4.8	Variation of mobility with sheet charge density	37

4.9	Effect of various scattering mechanism on mobility	37
4.10	Velocity field characteristic of 0.25μm AlInN/InN HFET	38
5.1	Variation of threshold voltage with dopant layer thickness for MOSHFET in comparison to HFET	40
5.2	Variation of threshold voltage with oxide layer thickness	40
5.3	I-V Characteristics of 0.25μm AlInN/InN (a) HFET (b) MOSHFET	41
5.4	I-V Characteristics of 0.25μm AlInN/InN MOSHFET in comparison to HFET	42
5.5	Variation of drain current with gate to source voltage	43
5.6	Variation of drain current with gate length	43
5.7	Variation of Transconductance with gate to source voltage	44
5.8	Variation of Transconductance with gate length	45
6.1	Variation of cut off frequency with gate source voltage for (a) HFET (b) MOSHFET	47
6.2	Variation of cut off frequency with gate to source voltage of MOSHFET in comparison to HFET	47
6.3	Variation of cut off frequency with gate length	48
6.4	Variation of cut off frequency with drain current	48

Nomenclature

d	polarization vector
d_c	thickness of cap layer (nm)
d_d	thickness of barrier (nm)
d_s	thickness of spacer layer (nm)
$e31$	piezoelectric coefficients
$e33$	piezoelectric coefficients
E_c	critical electric field (KV/cm)
ΔE_C	conduction band offset (eV)
f_t	cut-off frequency (GHz)
g_m	transconductance (mS/mm)
$G(q)$	form factor
I_{ds}	drain current (mA/mm)
K	Boltzman constant (JK^{-1})
K_F	Fermi wave vector
L_g	gate length (μm)
m	mole fraction
N_{back}	background donor density
N_D	doping concentration (cm^{-3})
N_T	carrier trap density (cm^{-3})
n_s	sheet carrier concentration (cm^{-2})
P	Piezoelectric polarization vector
P_{SP}	spontaneous polarization (Cm^{-2})
P_{PZ}	piezoelectric polarization (Cm^{-2})
P_0	form factor
q_{TF}	Thomas-Fermi screening wave vector
T	stress tensor
T	temperature (K)
U_{AL}	alloy potential
V_{ds}	drain to source voltage (Volt)

V_{gs}	gate to source voltage (Volt)
v_s	saturation velocity ($cmsec^{-1}$)
V_{th}	threshold voltage (Volt)
$V_c(x)$	channel potential (Volt)
W	gate width (μm)
x	distance (μm)
Σ	polarization induced charge density (Cm^{-2})
Φ_B	schottky barrier height (eV)
c	dielectric constant
μ	mobility ($cm^2V^{-1}sec^{-1}$)
ΔP_{sp}	Polarization discontinuity
ε_x	strain components along x direction
ε_y	strain components along y direction
Ω_0	volume occupied by one atom

Chapter I

Introduction

1.1 Overview

Development of microwave devices and circuits did not gain the same attention as Silicon (Si) based devices for digital applications until the 1980's because of the lack of commercial applications. The need for high performance devices has distinguished microwave devices from those geared toward digital applications. There are many areas where Si and other conventional semiconductor materials are not suitable due to the fundamental physics limitations. III-V semiconductor materials look increasingly attractive for many potential applications, where high electron mobility and high current carrying capabilities make them superior to silicon semiconductor technology [1]. Microwave and wireless devices have relied on III-V semiconductors since 1960's when the GaAs MESFET was announced by Mead [2]. GaAs has significant advantages over Si for high speed devices because of higher electron mobility. This advantage was further advanced by the ability to grow heterostructures. Heterojunction field-effect transistors (HFETs) have been considered as the most promising candidate for microwave high performances and low-noise applications due to its unique heterojunction material structure.

It has recently been the subject of much research effort to improve the high frequency performance of microwave FET. To achieve both high frequency and high performance in the microwave frequency range, the devices typically should have the following major characteristics: a) good confinement of carriers to the channel, b) high sheet charge density, c) high electron mobility and velocity, d) low parasitic capacitances and resistances and e) very short transit time. Recent studies show that reduction of gate length and increase of electron saturation velocity are the ways to improve the cut-off frequency [3]. Reduction of gate length has proved its effectiveness to improve the cut-off frequency of microwave FETs. However, reduction of gate length is limited by the saturation of electron drift velocity, short channel effect and heating effect [4, 5]. Gate scaling process

has become saturated. These limitations have allowed the implementation of novel device concept and development of new high frequency devices.

Indium nitride (InN) as a promising III-nitride semiconductor with many potential applications has attracted much attention recently owing to its superior electron transport properties [6, 7]. InN is predicted to have the lowest effective mass for electrons ($0.11m_0$) in comparison with AlN ($0.40m_0$) and GaN ($0.20m_0$) which is required for high mobility, high saturation velocity and scattering mechanism to be less effective. The saturation velocity is much larger than that of GaAs and GaN over a wide range of temperature of 150 K to 500 K and a doping concentration up to 10^{19} cm^{-3} [8]. Indeed, the existence of electrons in InN with velocities up to 2×10^8cm/sec is found [9], which is significantly higher than those observed for other conventional semiconductors. Figure 1.1 shows the velocity-field characteristics associated with wurtzite GaN, InN, AlN, and zincblende GaAs. The critical field at which the peak drift velocity was achieved for each velocity-field characteristic is clearly marked. It can be seen that each of these III-nitride semiconductors achieves a peak in its velocity-field characteristic. InN achieves the highest steady-state peak drift velocity of 4.2×10^7 cm/s [10]. This contrasts with the case of GaN, 2.9×10^7 cm/s, AlN, 1.7×10^7 cm/s and of GaAs, 1.6×10^7 cm/s [11]. These inherent properties of InN are very suitable for the design of high performances electronic devices. It was shown that InN-based FETs have an extremely high speed with a cutoff frequency of over 1 THz for 0.1 μm gates [12].

In addition to above mentioned properties the InN-based materials also exhibit strong lattice polarization effects [13]. Due to the piezoelectric and spontaneous polarization fields, InN-based HFETs have the ability to achieve two dimensional electron gas (2DEG) with sheet carrier densities of the order of 10^{14} cm^{-2} [14]. This mechanism of polarization leads to unprecedented high current drive capability that is one order of magnitude higher than their silicon or GaAs counterparts [15, 16]. Therefore, from the above-explained electron transport properties it can be concluded that InN is a highly potential material for the fabrication of high-performance HFET.

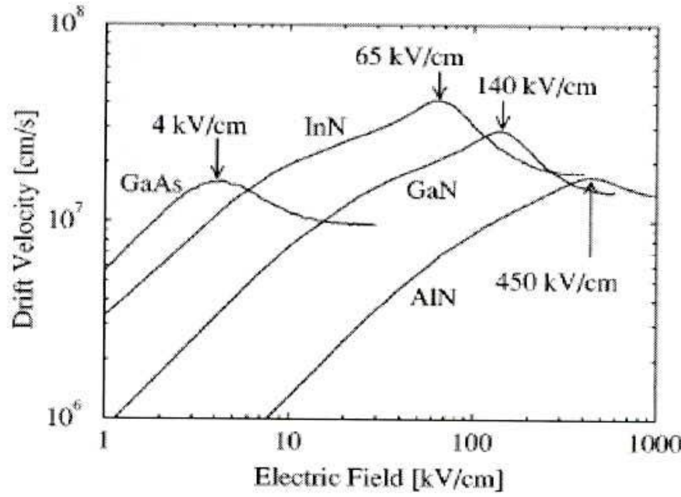

Fig. 1.1. The velocity-field characteristics associated with wurtzite GaN, InN, AlN, and Zincblend GaAs. In all cases, the temperature was set to 300K and the doping concentration was set to 10^{17} cm^{-3}. The critical fields at which the peak drift velocity was achieved for each velocity-field characteristic are clearly marked; 140 kV/cm for GaN, 65 kV/cm for InN, 450 kV/cm for AlN, and 4 kV/cm for GaAs.

1.2 Motivation and Objectives

The recent achievement in the InN research indicates that the InN film almost meets the requirements for application to practical devices. A remarkable improvement in the growth of InN film has been revealed through different scientific publications. High quality single crystalline InN film with two-dimensional (2D) growth and high growth rate can easily be obtained now. However, compared with other nitride based devices the progress in designing and fabrication of InN-based devices are at initial stage. In order to realize future high performance InN-based devices, understanding of detail device modeling and performance evaluations is urgently required. There have been very little works on InN-based devices. Recently, the effect of polarization on carrier confinement in InN-based heterostructure and calculation of the 2DEG concentration in InN-based heterostructures are reported [17-27]. However, these papers lack very important issues. Which also don't provide clear perception about the physical operation of the InN-based FET. Most of these models take the approximation of constant Fermi energy level, which transforms into a linear dependence of sheet charge density (n_s) on gate to source voltage (V_{gs}). But a linear n_s–V_{gs} relation fails in the near threshold and deep saturation regions [28-31]. The region near threshold, where carrier density is quite low, is very important for circuit operation in VLSI circuit design and hence demands special attention. The effect of gate voltage (V_g)

on n_s is also not shown. So a charge control model is essentially required to get an insight into the physical operation of InN-based device.

The development of new generation field-effect transistors (FETs) requires low gate leakage and superior pinch-off characteristics [32]. Recently, several groups have attempted to achieve gate leakage suppression and superior pinch-off characteristics by using the metal-insulator-semiconductor HFETs (MISHFETs) [33, 34] or metal-oxide-semiconductor HFETs (MOSHFETs) [35]. The built-in channel of MOSHFET is formed by the high density 2DEG at specific interface of InN-based heterostructures. However, in contrast to HFETs, the metallic gate is isolated from the barrier layer by a thin SiO_2 film. This insulator layer provides extremely low gate leakage current and allows for a large gate voltage swing (GVS) [36]. Thus MOSHFET combines the advantages of the MOS structure that suppresses the gate leakage current and heterointerface, which provides high-density high-mobility 2DEG channel.

In this work, InN-based HFETs without and with an oxide layer beneath the gate have been studied for high performances. A quantum mechanical charge control model based on self-consistent solution of Schrodinger-Poisson equations is developed to study the performance. To get an insight into the physical operation and carrier control mechanism of InN-based HFET this model is applied to investigate the quantum confinement of carriers and the effect of applied gate voltage on the carriers. The model includes the effect of gate voltage on Fermi energy which makes the model more accurate. To characterize the dc and high frequency performance a nonlinear analytical model is also presented in this dissertation. The highly dominant effect of spontaneous and piezoelectric polarization is incorporated in the present model to accurately predict the 2DEG sheet charge density at the AlInN/InN interface. The effects of parasitic source drain resistances and velocity saturation have also been included to accurately develop the dc model. To generalize the model, the pulse-doped structure comprising the schottky cap layer, dopant layer, and spacer layer is employed. The model is extended to calculate small signal parameters, viz. transconductance and unity current gain cut-off frequency, so as to predict the microwave performance of device.

1.3 Outline of Dissertation

Chapter 2 provides the background on the devices and materials investigated in this work. The electronic properties of III-nitrides are discussed, mainly focusing on polarization in the materials and its impact on the operation and modeling of heterojunction FETs. Finally a discussion of the state of the art in AlInN/InN HFETs is presented.

Chapter 3 presents a self consistent charge control model of Schrödinger-Poisson equations to calculate the charge density of AlInN/InN HFET's. Finally, a nonlinear analytical model is presented to characterize the dc and microwave performance of AlInN/InN MOSHFET structure.

Chapter 4 outlines the transport properties of AlInN/InN HFET's. This chapter describes the self consistent solution of Schrödinger and Poisson equations. A details study of channel formation in HFET, conduction band profile and the sheet carrier concentration for the 2DEG are presented. The mobility and drift velocity of the carrier in the proposed device considering relevant scattering mechanism are also described.

Chapter 5 shows DC characteristic of the AlInN/InN HFET. A detail study of charge control parameters such as threshold voltage and I-V characteristic is presented. Then, transconductance and the dependency of these parameters on gate length are also discussed.

Chapter 6 discusses the high frequency characteristics of the proposed device.

Chapter 7 summarizes the results from this research and provides guidelines for future work.

Chapter II

Background Information

2.1 Introduction

This chapter presents the background material pertaining to the modeling of devices that will be investigated. The chapter starts with a discussion of the electronic properties of III-nitrides, mainly focusing on polarization in the materials and its impact on the operation and modeling of heterojunction FETs. It is followed by an overview of the current status of InN FET development. The devices considered in this discussion are the AlInN/InN HFET and MOSHFET. The chapter ends with a discussion of the various approaches that can be taken to develop a large signal model for a device and the approaches that have been taken until now to develop models for InN FETs.

2.2 Polarization in III-nitride materials

In this section, the basic equations required to calculate polarization in strained III-nitride layers are presented and the impact of polarization on charge control in HFETs is discussed. Most of the material in this discussion on polarization in III-nitride semiconductors and devices is derived from [37-41]. Wide bandgap III-nitrides can exist in wurtzite (WZ) and zincblende (ZB) crystal structures. The wurtzitic structure is the predominant form for semiconductor device applications with the discussion in this chapter specifically referring to this. The wurtzite crystal is tetrahedrally coordinated and lacks inversion symmetry in the unit cell [37]. As a result, the crystals exhibit strong piezoelectric effects when strained along [0001] direction. In addition to piezoelectric effects, wurtzite InN has spontaneous polarization even in the absence of strain. The piezoelectric effect arises from lattice mismatch strain and thermal strain caused by the thermal expansion coefficient difference between the substrate and the epitaxial layers.

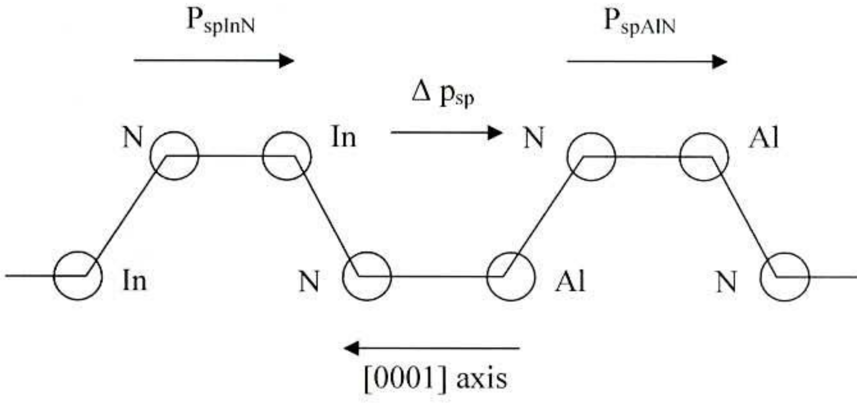

Figure 2.1: An illustration of the convention used to determine polarity in wurtzitic nitride films. The figure shows a In(Al)-polarity crystal with the bonds parallel to c-axis (horizontal in the diagram) going the cation (In or Al) to anion (N). The direction of spontaneous polarization in InN and AlN is also shown with the higher magnitude of polarization in AlN represented by the length of the arrow. Polarization discontinuity at the interface between the two crystals is represented by ΔP_{sp} and leads to a positive polarization charge

The presence of defects in a crystal can reduce strain and lower the strength of piezoelectric polarization. Polarization is dependent on the polarity of the crystal [38]. The polarity of a crystal depends on whether the bonds along the c-direction are from cation (In) to anion (N) sites or vice versa. The convention used in setting up all polarization related equations is that the [0001] axis points from the face of the N plane to the In plane, and marks the positive z direction. When the bonds along the c-direction are from the cation to anion atoms, the crystal is said to be In polarity and the direction of the bonds from In to N along the c-direction marks the [0001] direction. In N polarity crystals the bonds along the c-direction are from the N to In atoms and marks the -z direction. This is illustrated in figure 2.1. Polarization along the [0001] axis is of primary interest for device design because this is the direction along which epitaxial films and heterostructures are currently grown. Let the spontaneous polarization and piezoelectric polarizations along the c-axis of the wurtzite crystal be denoted by $P_{SP}(z)$ and $P_{PZ}(z)$, z refers to the unit normal vector along the c-axis (positive along [0001] direction). Using ab-initio methods, Bernardini et. al. [39] calculated the spontaneous polarization charge in AlN, GaN and InN to be -0.081, -0.029 and -0.032 C/m^2. Piezoelectric polarization vector is given by the dot product of the piezoelectric and stress tensors and can be written as $P = d. T$, where d is the

polarization vector and T is the stress tensor. In wurtzitic symmetry, the number of independent components of d reduces to three: e_{15}, e_{13} and e_{33}. [37]. The index 3 refers to direction of c-axis and in structures with growth along [0001] axis only the e_{31} and e_{33} components are important. The piezoelectric coefficients e_{33} and e_{13} can be used to calculate the piezoelectric polarization using [38]:

$$P_{PE} = e_{33}\varepsilon_z + e_{31}(\varepsilon_x + \varepsilon_y) \tag{2.1}$$

Where ε_x and ε_y are the in-plane strain components and ε_z is the out of plane component. The in-plane strain is assumed to be equal in both directions and is given by

$$\varepsilon_x = \varepsilon_y = \frac{a - a_0}{a_0} \tag{2.2}$$

where a_0 is the equilibrium value of the in-plane lattice parameter. The relation between this lattice constant a_0 and c_0 are is given as

$$\frac{c - c_0}{c_0} = -2\frac{C_{13}}{C_{33}}\frac{a - a_0}{a_0} \tag{2.3}$$

Where, C_{13} and C_{33} are elastic constants. Using equations 2.1 and 2.3 the amount of piezo-electric polarization in the direction of the c-axis can be determined by

$$P_{PE} = 2\frac{a - a_0}{a_0}(e_{31} - e_{33}\frac{C_{13}}{C_{33}}) \tag{2.4}$$

The values of constants required to calculate polarization in the three nitride materials are given in Table 2.1. For the In face crystals, the piezoelectric polarization in AlInN is negative for tensile ($a > a0$) strain and positive for compressive strain. Since the in-plane lattice parameter of InN (a_{InN} is larger than that of AlN (a_{AlN}), the AlInN layer in an AlInN/InN system is in tensile strain and piezoelectric polarization is negative. Therefore, in a In polarity crystal, the net polarization in AlInN points toward the interface and is

larger in magnitude than the polarization in InN. Applying Gauss's law at the interface, it can be shown that a net fixed positive sheet charge forms at the interface (see figure 2.2). This aids the formation of the sheet charge at the heterointerface.

Table 2.1: Spontaneous polarization, piezoelectric coefficients, elastic constants and c-plane lattice constants of InN, AlN and GaN. Data taken from [38 - 40]

wurtzite	InN	AlN	GaN
Psp (c/m^2)	-0.032	-0.081	-0.029
e_{31} (c/m^2)	0	1.55	1
e_{33} (c/m^2)	-0.57	-0.60	-0.49
C_{13} (GPa)	92	108	103
C_{33} (GPa)	224	373	405
a (A^0)	3.54	3.112	3.189

For AlInN and InGaN alloys, the values of spontaneous polarization, lattice constant, piezoelectric constants and elastic constants are calculated by linear interpolation between the values of the constants for AlN(InN) and GaN

$$C(x) = C_{AlN}x + C_{InN}(1 - x) \qquad (2.5)$$

where C is the constant being calculated.

From the discussion above, the amount of polarization in AlInN can be controlled by changing the mole fraction of Aluminum in AlInN to control the sheet charge density in the electron gas. For layers thicker than a critical value, strain relaxation occurs which leads to a reduction in piezoelectric polarization. This has to be taken into account while modeling devices with a high Al mole fraction in the barrier layer of an HFET.

2.3 Charge Control in an HFET

The cross section of a simplified HFET structure is shown in figure 2.3. The corresponding band diagram for the HFET is shown next to the device cross section. Although more

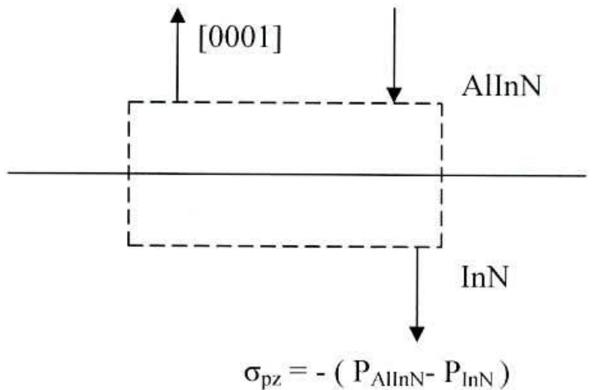

Figure 2.2: Polarization charge at the AlInN/InN interface. The positive z axis points along the [0001] crystallographic axis which points upwards for In face crystals. Polarization fixed charge is given by the negative gradient of polarization which creates the positive sheet charge at the interface in case of AlInN/InN heterojunction.

complicated structures are used in real devices, this figure illustrates the basic principles of an HFET quite clearly. The doped barrier layer forms a heterointerface with the undoped buffer layer underneath. As a result of the conduction band discontinuity, a quantum well forms at the interface and charge transfers from the barrier layer to the quantum well in the buffer layer. Charge control is achieved by placing a metal Schottky gate on top of the barrier layer that modulates the depletion region in the barrier layer. Below threshold, the sheet charge is fully depleted. Under normal operating conditions, the barrier layer is fully depleted and the channel layer is screened by the formation of the sheet charge at the interface. As the gate bias is increased, charge transfer into the barrier layer takes place as hot electrons in the channel can overcome the conduction band discontinuity. An accurate description of the charge control in an HFET requires a self consistent solution of the Schroedinger and Poisson equations at the heterojunction. When the De Broglie wavelength of electrons is of the same order as the dimensions of the well formed by conduction band bending at the heterointerface [42], energies are quantized. A detailed discussion of the electronic properties of two dimensional systems can be found in [43].

Khulna University of Engineering & Technology
KUET
Bangladesh
Central Library

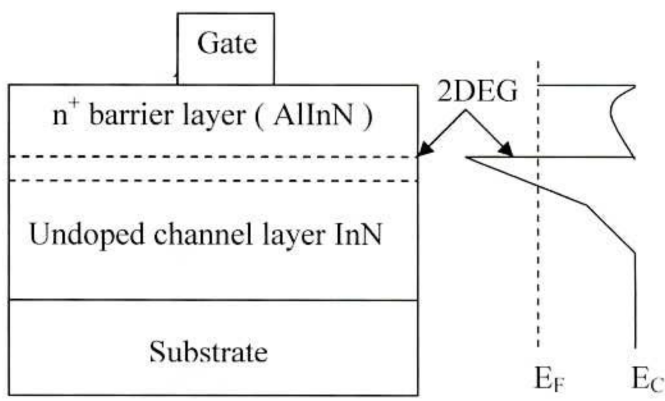

Figure 2.3: Cross section of an HFET: The corresponding band diagram is drawn next to it, illustrating the formation of the quantum well at the heterojunction.

2.4 Impact of polarization on sheet charge density

The Initial works of Kong et al. and Hassan et al. [25], [23] showed that polarization fields are the cause for the high sheet charge density observed in InGaN/InN HFETs and AlInN/InN. It is now accepted that polarization fields are the driving force that lead to the accumulation of free carriers in the quantum well [44]. This has been shown by various works that the sheet charge at AlGaN/GaN interfaces can be calculated using a self consistent solution of the Schroedinger Poisson equations [45], [46]. The impact of polarization fields on the conduction band potential has to be taken into account in the Schroedinger equation [44]. Freeman presents the necessary equations required to solve the Schroedinger and Poisson equations while taking into account local stress variation throughout the structure. Jogai and Sacconi's works [45], [46] go through the self consistent solution for AlGaN/GaN HFETs. Both works indicate the importance of polarization fields in creation of the sheet charge at the interface. Jogai's work also indicates that the polarization charge itself does not act as conventional dopant atoms supplying free charge for conduction in the quantum well. Instead, it acts as the driving force that leads to accumulation of free charge in the quantum well. The free charge can be

provided by a doped barrier layer (which is the case in the devices studied in this work), surface donor levels as proposed by Ibbetson et. al. [47] or from unintentionally doped barrier layers due to intrinsic defects and impurities in the as grown materials.

2.5 AlInN/InN HFETs

HFET's with InN channels and AlInN barriers are predicted to outperform GaAs-based HFET's for frequency response [48]. They will have - 50% higher average electron transit velocity [49]. They will also have three times as high drain-source breakdown voltage, due to their 1.2 MV/cm electric field strength [50]. In combination, the GaN HFET Johnson figure of merit, in the form P f^2_t Z load, is ~20 times as high as for GaAs HFET's [48]. Together, the expected electron mobility [51] of ≥ 3,000 cm^2/V-s, due to low electron effective mass ($0.11m_0$), and an 2DEG sheet density of ≥ 1 x $10^{13}/cm^2$, will yield 200 Ω/sq. sheet resistance, which is half that of GaN HFET's [48].

2.6 Issues Facing AlInN/InN HFETs

1. Dispersion

The reduction in microwave power output is related to an observed reduction in drain current measured under RF drive as compared to DC characteristics. Maximum power obtainable from a device in class A mode of operation can be given by

$$P_{max} = I_{max} (V_{breakdown} - V_{knee})/8 \qquad (2.6)$$

As 2.11 indicates, the maximum power drive can degrade either through a decrease in the maximum saturation current from the device or because of an increase in the knee voltage. This is commonly referred to as "current slump" or "current collapse". This phenomenon is commonly attributed to the presence of surface traps in the gate drain access region which leads to the formation of a "virtual gate" as carriers trapped in the region deplete the channel underneath [52-53]. Others have attributed this to buffer layer trapping wherein

hot electrons under a high drain bias escape from the 2DEG and get trapped in the buffer layer traps [54-56]. Another effect of dispersion in current-voltage characteristics is a frequency dependent output conductance that increases at high frequencies and a reduced transconductance at high frequencies [57]. The transition frequency can range from 1Hz to 1 MHz depending on the time constants involved in electron capture and emission processes. Both effects have a detrimental impact on the linear gain obtainable from the device. It has also been observed that the RF breakdown voltages are lower than the DC values. This has been attributed to the formation of charge dipole domains at the gate drain edge under high field (high voltage) operation [58].

2. Thermal Effects

Accurate thermal modeling of InN devices is of critical importance because of the high power density that these devices are expected to operate under. Thermal effects degrade the performance of a device through a reduction in low field mobility as well as high field saturation velocity. Currently, most InN devices are fabricated on sapphire substrates because of the relatively low cost. Sapphire has a thermal conductivity of 0.48 W/(K.cm) and thermal effects are very significant. SiC has a thermal conductivity of 3.2 (W/K.cm) which can lead to much better power dissipation through the substrate. This has been borne 4 times the rise in a device on SiC [59]. Other materials with better thermal conductivity than sapphire being investigated for use as substrates are AlN, Si and GaN could potentially replace sapphire for high power applications.

2.7 Dielectrics for InN MOSHFETs

The basic electrical requirements for a compatible dielectric to any semiconductor in the fabrication of MOSFETs are a high dielectric constant, large bandgap, large conduction band offset and a high quality interface with a low interfacial state density D_{it}. For development of MOSHFETs a compatible gate dielectric that forms an interface with low density of trapping states with the underlying semiconductor is required. A high density of interface states leads to a pinning of the Fermi level. Fermi level pinning occurs when the density of interface states is large enough to exchange charge with the underlying

semiconductor without allowing the gate to control the conducting channel in the device. The states also trap charge and cannot respond to high frequency signals which lead to the dispersion characteristics observed in HFETs. Traditionally, this has been difficult to achieve for III-V semiconductors such as GaN due to chemical and structural defects that are present at the interface. The development of dielectrics for InN FETs is very similar to the path followed in the attempt to develop dielectrics for GaN MOSFETs.

A high dielectric constant is desirable as it increases the gate capacitance which leads to a better channel control. In recent years, the development of high κ dielectrics has been the focus in silicon research due to device scaling into nanoscale dimensions. Most of the dielectrics that are investigated for III-V material systems have a higher dielectric constant than SiO_2. However, development of high κ dielectrics has faced significant roadblocks due to the difficulties in incorporating them into the silicon MOSFET process flow.

High conduction band offsets and a large band gap are essential to reduce gate leakage via the thermionic emission, and Fowler Nordheim tunneling mechanisms. A high interface state density can also increase leakage through a trap assisted tunneling mechanism.

The development of InN MOSHFETs is motivated by several advantages when compared to AlInN/InN HFETs and Si RF CMOS devices for high frequency applications, which are listed below:

1. True enhancement mode operation with a single power supply for circuit applications, thus increasing power efficiency.

2. The higher saturation velocity of InN provides a higher ft·Lg product than Si. Also, it has been shown that the overshoot velocity in InN is much higher than the steady state peak velocity for a given field value and extends over a longer distance [60]. This can be exploited for the design of short channel devices wherein the velocity overshoot phenomenon can be observed under switching electric fields.

3. High quality dielectric layers can reduce dispersion issues and hence, the linearity of InN MOSHFET's can be higher.

5. Forward swing on the gate limited by the breakdown process unlike in a HFET, which is limited by the Schottky diode turn on. The drain current of a FET can be written as

$$I_{DS} = \frac{W}{L} \mu \, n \, C_i \, (V_g - V_T) \, \frac{dV_c(x)}{dx} \qquad (2.7)$$

For a given gate periphery, the drain current drive of a MOSHFET can be higher than that of a HFET because of the increase in channel carrier density, which is modified by the surface states [61].

2.8 Modeling of FETs

2.8.1 Empirical Models

Most of the popular models used for circuit design in CAD tools are empirical models such as the BSIM series models for MOSFET's, Materka, Curtice, and TOM models for MESFET's and HFET's. The popularity of these models stems from the fact that they are easily implemented in a circuit simulator and are simulated quickly, which is essential for circuit design. The current-voltage and capacitance-voltage characteristics are represented by some combination of non-linear functions such as power series (Cubic Curtice being an example) and hyperbolic functions (Angelov model). In general, these models are capacitance based with the nonlinear capacitances being defined as a function of the terminal voltages. Although the simulation for a well extracted model can be very accurate, the model itself does not have predictive properties and a new model has to be extracted every time a new device or process is to be used. Scaling properties of these models are also not well defined and precautions have to be taken when using devices of a different size than what was used to extract the model.

2.8.2 Table Based Models

Table based models were developed by Root [62] to model high frequency devices. These models use smooth interpolating functions to generate missing data between measured data points for the DC current-voltage and high frequency behavior of a device. These models are generic and can be used to model any FET device once formulated. However, they do not have any predictive properties and a large number of measurements are required to model non-linear characteristics accurately.

2.8.3 Physics Based Models

Physics-based models are based on a physical description of the device. An accurately formulated analytical description can be used to predict device performance before measured data is available. Self-consistent calculation solving 1-D Schrodinger's and Poisson's equation simultaneously has been shown to give qualitative agreement with the experiment results for the charge control in an HFET.

In this dissertation a self consistent charge control model based on 1-D Schrödinger-Poisson equations over the entire device structure is developed. Then a nonlinear analytical model to characterize the dc and high frequency performance of AlInN/InN HFET without and with an oxide layer beneath the gate is also described. The mobility and the velocity-field characteristics are obtained using Monte Carlo simulation. The simulation model incorporates an analytical 3-valley band structure with non parabolicity for all nitride materials. The developed model is employed to study the impact of device performance on various parameters.

Chapter III

Modeling of HFET

3.1 Introduction

To characterize and optimize the device performance, an accurate charge control relation between 2DEG sheet carrier density (n_s) and the controlling gate voltage (V_{gs}) is desirable. This chapter starts with a self consistent charge control model of AlInN/InN HFET using Schrödinger-Poisson equations. Then describes a nonlinear analytical model to characterize the dc and microwave performance of the proposed device incorporating an oxide layer between the barrier and gate contact. This developed model is employed to study the impact of device performance on various parameters.

3.2 Device Structure

The basic structure of the proposed InN based HFET without and with an oxide layer is shown in Fig. 3.1. It consists of a substrate, an undoped InN layer to form 2DEG channel, an undoped AlInN spacer layer of thickness d_s, a n-doped AlInN layer of thickness d_d to provide 2DEG sheet carrier density, and an undoped schottky cap layer of thickness d_c. The source and drain electrodes are ohomic contacts while the gate electrode which modulates the charge in the conducting channel is a schottky barrier placed on the undoped AlInN cap layer (d_c) of 10 nm. The thickness of n-doped AlInN barrier layer (d_d) and undoped AlInN spacer layer (d_s) are 10 nm and 2 nm, respectively. The thickness of the channel is assumed to be 1 μm and doping density of AlInN is taken to be 2×10^{18} cm^{-3}. The value of aspect ratio (ratio of gate length to barrier thickness) is considered 25 for 0.25 μm gate length. The high frequency performance is significantly deteriorated by short channel effect if the aspect ratio is less than 5 [63-64]. Improvement in the model is accomplished by keeping the high aspect ratio. Incorporating an oxide layer beneath the gate contact, the model also combines the advantages of the MOS structure that suppresses

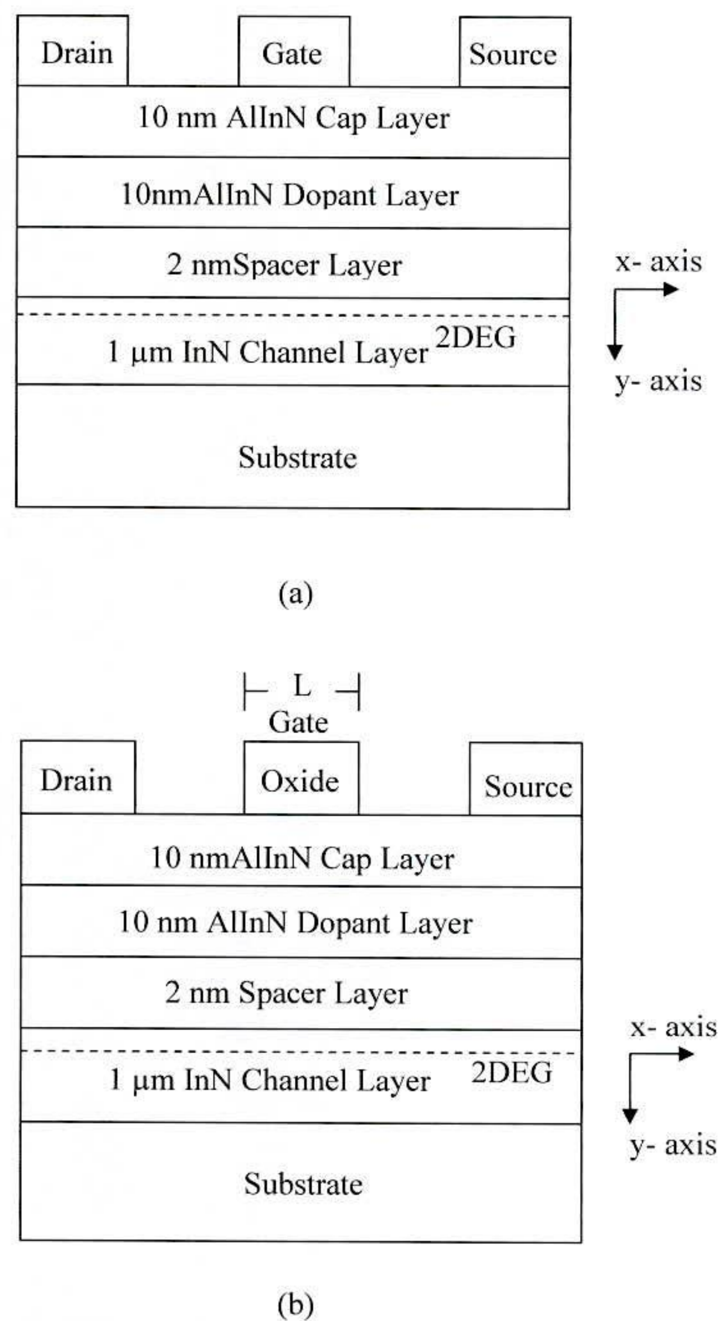

Figure 3.1: Schematic view of the proposed InN based (a) HFET (b) MOSHFET

the gate leakage current and AlInN/InN heterointerface, which provides high-density high-mobility 2DEG channel. A thin film of SiO_2 of thickness t_{ox} and dielectric permittivity ε_m is deposited beneath the gate.

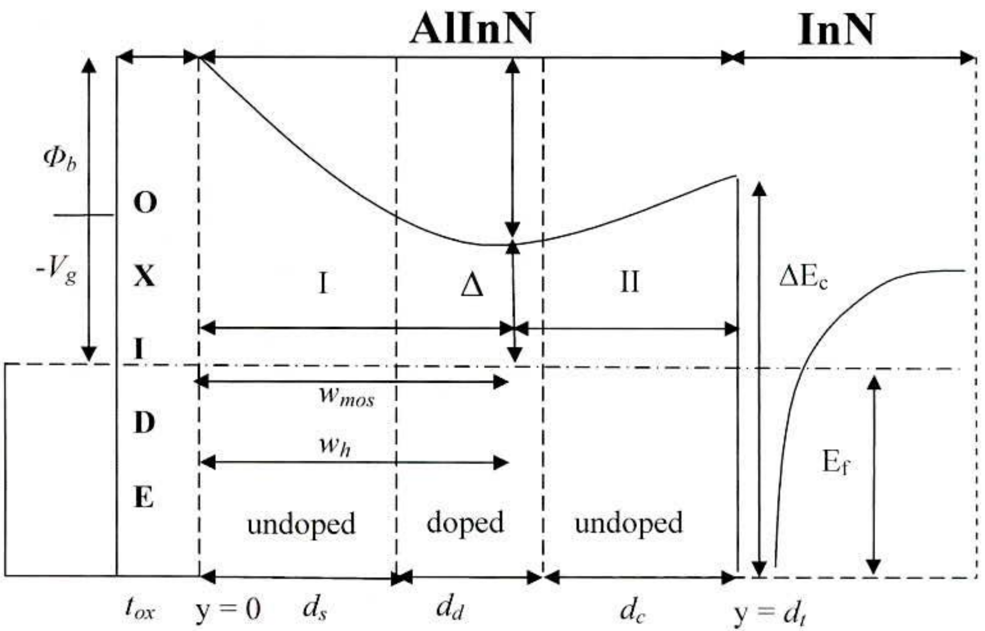

Figure 3.2: Conduction band profile of AlInN/InN based MOS hetrostructure along the y-axis

3.3 Charge Control Model

To study the charge control it is necessary to examine in detail the band profile of the proposed device. A band diagram of the structure defining the various quantities and symbols that are used in the model are shown in Fig. 3.2. An accurate solution of free charge in the device requires a self consistent solution of the Schrödinger and Poisson equations over the entire device structure. In this thesis work a quantum mechanical charge control model using the self-consistent solution of Schrodinger-Poisson equations is described. This model is applied to investigate the sub band states, quantum confinement of carrier and the effect of applied gate voltage on the carrier in order to get an insight into the physical operation and carrier control mechanism of InN-based HFET. The model includes the effect of polarization and the effect of gate voltage on Fermi energy which makes the model more accurate. The AlInN/InN HFET structure used for this thesis is shown in Fig 3.1. The model first obtains the potential profile in the HFET structure by solving the Schrödinger equation and Poisson equation self-consistently. The Schrödinger equation yields the confined charge terms in the Poisson equation which, in turn,

determines the potential profile. This potential profile is fed back into the Schrödinger equation until the solution of Poisson equation goes to convergence. According to the effective mass approximation, the one dimensional Schrödinger equation is given by

$$\frac{\hbar^2}{2}\frac{d}{dx}\left[\frac{1}{m^*}\frac{d\psi_i(x)}{dx}\right]+V(x)\psi_i(x)=E_i\psi_i(x) \tag{3.1}$$

where m is the effective mass, Ψ_i is the wave function of the i th sub band and is found from the solution of Schrodinger equation couple with Poisson's equation, E_i is the energy of i th subband. The unknown potential energy $V(x)$ is given by

$$V(x)=-q\phi(x)+\Delta E_c(x) \tag{3.2}$$

q is the electronic charge, $\Delta E_c\ (x)$ is the conduction band offset and $\phi(x)$ is the electrostatic potential and is found from the solution of Poisson's equation, expressed as

$$\frac{d}{dx}\left[\varepsilon\frac{d\phi(x)}{dx}\right]=-q[N_D^+ + p(x)-n(x)-N_A^-] \tag{3.3}$$

where ε is the dielectric constant, N_D^+, $p(x)$, $n(x)$, N_A^+, are the density of ionized doping donors, free holes, free electrons, and ionized doping acceptors. In the simulation region we assume $N_A^+ = p(x) = 0$ and the inherent electron accumulation at InN surface due to the effects of surface charge and dislocation densities is not considered. For AlInN/ InN material, we must take account of the polarization sheet charge at the interface in Poisson's equation, and the boundary condition is

$$E_{Al_mIn_{1-m}N}\varepsilon_{Al_mIn_{1-m}N}-E_{InN}\varepsilon_{Inn}=-\sigma \tag{3.4}$$

where E is the electric field, ε is the dielectric constant and σ is the bound polarization induced charges at the surface of AlInN , interface of AlInN / InN. σ (y) is given by

$$|\sigma(x)|=|P_{pz}(Al_mIn_{1-m}N)+P_{sp}(Al_mIn_{1-m}N)-P_{sp}(InN)| \text{ C/m}^2 \tag{3.5}$$

where $P_{pz}(Al_mIn_{1-m}N)$ and $P_{sp}(Al_mIn_{1-m}N)$ are given by Ambacher et al.[65]

$$P_{pz}(Al_mIn_{1-m}N) = [-0.28m+0.104m(1-m)]\ C/m^2$$

$$P_{sp}(Al_mIn_{1-m}N) = -0.090m-0.042(1-m)+0.070m(1-m)\ C/m^2$$

$P_{sp}(InN) = -0.032\ C/m^2$ is given by [66]·

For the energy levels corresponding to the 2DEG, it is assumed that the 2DEG lies in an asymmetric potential well, with the first two sub bands i.e. first sub band, E_1 and second sub band, E_2 occupied. As the higher sub bands have the negligible effect, only first two sub bands are considered for the calculation. The total 2DEG sheet carrier concentration (n_s) is determined summing over the concentration n_i in each sub band;

$$n_s = \sum_{i=1}^{2} n_i = \sum_{i=1}^{2} \frac{m^*}{\pi\hbar^2} \int_{E_i}^{\infty} \frac{1}{1+e^{\left(E_i - E_F / kT\right)}} dE = \sum_i^2 \frac{m^* k_B T}{\pi\hbar^2} \ln[1+e^{\left(E_i - E_F / kT\right)}] \tag{3.6}$$

where k_B is the Boltzman constant, T is the temperature and E_F is the Fermi level, which can be expressed in terms of E_i and n_s as follows [67]

$$E_F = \frac{n_s}{2D} + \frac{1}{2}\sum_{i=1}^{2} E_i \tag{3.7}$$

where D is the density of states and is given by $D = \frac{qm^*}{2\pi\hbar^2}$ (3.8)

The free electron distribution is given by

$$n_s(x) = \sum_{i=1}^{2} |\psi_i(x)|^2 n_i \tag{3.9}$$

Substituting the calculated $n_s(x)$ into Eq. 3.6, the new electrostatic potential $Ø(x)$ can be obtained, and thus a revised potential $V(x)$, which is fed back into the Schrodinger equation until this solution of Poisson equation goes on convergence. The calculation is done for T=300 K. The Schrodinger and Poisons equations are solved by well known finite difference method which is shown in appendix A.

3.4 Drain Current Modeling

When the gate voltage exceeds a certain level called threshold voltage, the channel is formed and contributes to conduction mechanism in the device. The expression for drain current in the channel is obtained from the following equation:

$$I_{ds}(x) = qwn_s(x)v(x) \tag{3.10}$$

where, q is charge of an electron, w is gate width, $v(x)$ is the carrier velocity and $n_s(x)$ is the 2DEG sheet charge density can be calculated according to Ref [68].

$$n_s(x) = \frac{\varepsilon_0 \varepsilon_s}{q(d_t + \frac{\varepsilon_s t_{ox}}{\varepsilon_{in}})}(V_{geff} - V_{th} - E_f) \tag{3.11}$$

where v_{geff} is the effective gate voltage and v_{th} is the threshold voltage. The model incorporates the nonlinear dependence of quasi Fermi level position E_f on sheet carrier density n_s using the following polynomial expression given by Ref. [68]

$$E_f = k_1 + k_2\sqrt{n_s} + k_3 n_s \tag{3.12}$$

where k_1 is the subthreshold factor, k_2 *is the linear factor* and k_3 is the saturation factor. the values of k_1, k_2 and k_3 are obtained using the effective mass of electron of AlInN/InN system following the same approach as proposed by Aggarwal et al. [68].The threshold voltage is determined by Aggarwal et al. [68]

$$V_{th} = \phi_b(m) - \Delta E_c - \frac{qN_d d_d^2}{2\varepsilon_0\varepsilon_s}(1+\frac{2d_s}{d_d}) - \frac{qN_d d_d t_{ox}}{\varepsilon_0\varepsilon_s} - \frac{\sigma_{pZ}(m)(d_t + \frac{\varepsilon_s t_{ox}}{\varepsilon_{in}})}{\varepsilon_s\varepsilon_0} + k_1$$

where, $\phi_b(m)$ is the schottky barrier height between bulk semiconductor and gate electrode, ΔE_c is the conduction band discontinuity, $\sigma_{pZ}(m)$ is the mole fraction dependent polarization induced charge, t_{ox} is the oxide layer thickness.

The velocity field relation in equation (3.9) is as follows:

$$v(x) = \frac{\mu E(x)}{1+\frac{E(x)}{E_c}} \quad \text{for} \quad E < E_c \tag{3.13a}$$

$$= v_{sat} \quad \text{for} \quad E > E_c \tag{3.13b}$$

where μ is mobility of electron, $E(x) = \frac{\partial V(x)}{\partial x}$ is the electric field at any point x in the channel, $E_c = \frac{v_{sat}}{\mu}$ is critical field due to velocity saturation, and v_{sat} is the saturation velocity.

1. Linear Regime

For lower drain voltages, average electron velocity is less than saturation velocity v_{sat}. Thus, substituting equation (3.13a) and (3.11) in equation (3.10) and integrating the equation from the source $x = 0$ to the drain side $x = L$, the drain current in the linear region is obtained as Ref []

$$I_{dsL} = \frac{q^3(d_t + \frac{\varepsilon_s t_{ox}}{\varepsilon_{in}})\mu w}{-16\varepsilon_s\varepsilon_0(q(d_t + \frac{\varepsilon_s t_{ox}}{\varepsilon_{in}}) + \varepsilon_s\varepsilon_0 k_3)^3} \times \left(\frac{f(y_1) - f(y_0)}{L + \frac{\mu(V_{ds} - I_{ds}(R_s + R_d))}{v_{sat}}} \right) \tag{3.14}$$

where R_s and R_d are the parasitic source and drain resistance and

$$f(y)=\left(\frac{\varepsilon_s\varepsilon_0 k_2}{q(d_t+\frac{\varepsilon_s t_{ox}}{\varepsilon_{in}})}\right)^2 y+\frac{y^2}{2}-\frac{4\varepsilon_s\varepsilon_0 k_2 y^{\frac{3}{2}}}{3q(d_t+\frac{\varepsilon_s t_{ox}}{\varepsilon_{in}})}$$

$$y_1=\left(\frac{\varepsilon_s\varepsilon_0 k_2}{q(d_t+\frac{\varepsilon_s t_{ox}}{\varepsilon_{in}})}\right)^2+\frac{4\varepsilon_s\varepsilon_0 k_2}{q(d_t+\frac{\varepsilon_s t_{ox}}{\varepsilon_{in}})}\left(1+\frac{\varepsilon_s\varepsilon_0 k_3}{q(d_t+\frac{\varepsilon_s t_{ox}}{\varepsilon_{in}})}\right)\times(V_{gs}-V_{th}-V_{ds}-I_{ds}R_s)$$

$$y_0=\left(\frac{\varepsilon_s\varepsilon_0 k_2}{q(d_t+\frac{\varepsilon_s t_{in}}{\varepsilon_{in}})}\right)^2+\frac{4\varepsilon_s\varepsilon_0 k_2}{q(d_t+\frac{\varepsilon_s t_{in}}{\varepsilon_{in}})}\left(1+\frac{\varepsilon_s\varepsilon_0 k_3}{q(d_t+\frac{\varepsilon_s t_{in}}{\varepsilon_{in}})}\right)\times(V_{gs}-V_{th}-I_{ds}R_s)$$

2. Saturation Regime

At the drain end of channel, the velocity becomes saturated at $V_{ds} = V_{dsat}$; then from equation (3.13b) and equation (3.11), we obtain the expression for drain saturation current as

$$I_{dsat}=\frac{qwv_{sat}}{4\left(1+\frac{\varepsilon_s\varepsilon_0 k_3}{q(d_t+\frac{\varepsilon_s t_{ox}}{\varepsilon_{in}})}\right)^2}\left(\left(\frac{\varepsilon_s\varepsilon_0 k_2}{q(d_t+\frac{\varepsilon_s t_{ox}}{\varepsilon_{in}})}\right)^2+y_{sat}-\frac{2\varepsilon_s\varepsilon_0 k_2\sqrt{y_{sat}}}{q(d_t+\frac{\varepsilon_s t_{ox}}{\varepsilon_{in}})}\right) \tag{3.15}$$

where

$$y_{sat}=\left(\frac{\varepsilon_s\varepsilon_0 k_2}{q(d_t+\frac{\varepsilon_s t_{ox}}{\varepsilon_{in}})}\right)^2+\frac{4\varepsilon_s\varepsilon_0}{q(d_t+\frac{\varepsilon_s t_{ox}}{\varepsilon_{in}})}\left(1+\frac{\varepsilon_s\varepsilon_0 k_3}{q(d_t+\frac{\varepsilon_s t_{ox}}{\varepsilon_{in}})}\right)\times(V_{gs}-V_{th}-V_{dsat}-I_{ds}R_s)$$

in which V_{dsat} is calculated numerically by equating equation (3.15) and (3.14) at $V_{ds} = V_{dsat}$ following the principle of current continuity.

3.5 Transconductance Model

For the optimization of FETs in high frequency applications, the transconductance (g_m) plays a significant role. It is one of the most important indicators of device quality for microwave applications and is evaluated as

$$g_m = \left.\frac{\partial I_{ds}}{\partial V_{gs}}\right|_{V_{ds}=const}$$

1. Linear Regime

Differentiating equation (3.14) with respect to gate source voltage, the transconductance in linear region is obtained as

$$g_m = -\frac{q\mu w}{16\dfrac{\varepsilon_s\varepsilon_0}{q(d_t+\frac{\varepsilon_s t_{ox}}{\varepsilon_{in}})}\left(1+\dfrac{\varepsilon_s\varepsilon_0 k_3}{q(d_t+\frac{\varepsilon_s t_{ox}}{\varepsilon_{in}})}\right)^3\left(L+\dfrac{\mu(V_{ds}-I_{ds}(R_s+R_d))}{v_{sat}}\right)} \times\left[\left(\frac{\partial f(y_1)}{\partial V_{gs}}-\frac{\partial f(y_0)}{\partial V_{gs}}\right)+\left(\frac{\mu g_m(R_s+R_d)(f(y_1)-f(y_0))}{v_{sat}(L+\frac{\mu(V_{ds}-I_{ds}(R_s+R_d))}{v_{sat}})}\right)\right] \quad (3.16)$$

where

$$\frac{\partial f(y_0)}{\partial V_{gs}} == \frac{4\varepsilon_s\varepsilon_0}{q(d_t+\frac{\varepsilon_s t_{ox}}{\varepsilon_{in}})}\left(1+\frac{\varepsilon_s\varepsilon_0 k_3}{q(d_t+\frac{\varepsilon_s t_{ox}}{\varepsilon_{in}})}\right)\left(\left(\frac{\varepsilon_s\varepsilon_0 k_2}{q(d_t+\frac{\varepsilon_s t_{ox}}{\varepsilon_{in}})}\right)^2+y_0-\frac{2\varepsilon_s\varepsilon_0 k_2\sqrt{y_0}}{q(d_t+\frac{\varepsilon_s t_{ox}}{\varepsilon_{in}})}\right)(1-g_m R_d)$$

and

$$\frac{\partial f(y_1)}{\partial V_{gs}} = \frac{4\varepsilon_s\varepsilon_0}{q(d_i + \frac{\varepsilon_s t_{ox}}{\varepsilon_{in}})}\left(1+\frac{\varepsilon_s\varepsilon_0 k_3}{q(d_i + \frac{\varepsilon_s t_{ox}}{\varepsilon_{in}})}\right)\left(\left(\frac{\varepsilon_s\varepsilon_0 k_2}{q(d_i + \frac{\varepsilon_s t_{ox}}{\varepsilon_{in}})}\right)^2 + y_1 - \frac{2\varepsilon_s\varepsilon_0 k_2\sqrt{y_1}}{q(d_i + \frac{\varepsilon_s t_{ox}}{\varepsilon_{in}})}\right)(1+g_m R_d)$$

2. Saturation Regime

Differentiating equation (3.15) with respect to gate source voltage, the transconductance in saturation region is obtained as

$$g_{msat} = \frac{q\mu w\varepsilon_s\varepsilon_0\varepsilon_{in}v_{sat}}{(d_i\varepsilon_{in} + \varepsilon_s t_{ox} + \varepsilon_s\varepsilon_0\varepsilon_{in}k_3)}\left(1-\frac{\varepsilon_s\varepsilon_0 k_2}{q(d_i + \frac{\varepsilon_s t_{ox}}{\varepsilon_{in}})\sqrt{y_{sat}}}\right)(1-g_m(sat)R_s) \quad (3.17)$$

3.6 Cut off frequency

The cut-off frequency f_t is an indicator of device's high frequency performance, and it determines the ultimate switching speed of the device. It is given as the ratio of transconductance g_m to the total gate capacitance C_{gT}, i.e.

$$f_t = \frac{g_m}{2\pi C_{gT}} \quad (3.18)$$

and is written by substituting the value of g_m from equation (3.16) and C_{gT}, the total gate capacitance, is calculated by the parallel combination of oxide capacitance C_{ox} and bulk capacitance C_b as follows:

$$C_{gT} = \frac{C_{ox}C_b}{C_{ox}+C_b}$$

where, $C_b = \frac{w\varepsilon_s\varepsilon_0 L}{d_i}$ and $C_{ox} = \frac{w\varepsilon_{in}\varepsilon_0 L}{t_{ox}}$ and wL denotes the effective area under the gate.

The parameters used in the DC and high frequency analysis at room temperature are listed in Table 3.1.

Table 3.1: Parameters used in the analysis

Parameters	Description	Value
T	Temperature	300 K
μ	Electron mobility	21×10^{2} cm^{2}/Vs
v_{sat}	Saturation velocity	4.5×10^{7} cm/s
m	Mole fraction	0.1
ΔE_c	Conduction band offset	2.7 eV
ε_0	Absolute permittivity	8.854×10^{-12} F/m
ε_s	Permittivity of AlInN	$14.18\varepsilon_0$
ε_{in}	Permittivity of oxide layer	$3.9\varepsilon_0$
Psp(m)	Spontaneous polarization at mole fraction m	-0.040 C/m^{2}
$\Phi_b(m)$	Barrier height	0.743 V
k_1	Subthreshold factor	-0.1794 V
k_2	Linear factor	2.991×10^{-9} V/m
k_3	Saturation factor	-0.657×10^{-18} V/m^{2}
q	Electronic charge	1.6×10^{-19} C
R_d	Parasitic drain resistance	1 Ω
R_s	Parasitic source resistance	0.5 Ω
m_0	rest mass of electron	9.1×10^{-31} kg

Chapter IV

Transport Properties

4.1 Introduction

To study charge control characteristics and channel mobility of a device it is needed to examine in detail the band profile and scattering theory in the device. The first section of this chapter describes the self consistent solution of Schrödinger and Poisson equations. A details study of conduction band profile and the sheet carrier concentration for the 2DEG are presented. The mobility and drift velocity of the carrier in the proposed device considering relevant scattering mechanism are described in the second part of this chapter.

4.2 Charge Control Characteristics

4.2.1 Conduction Band Profile

Schrödinger's equation is solved coupled with Poisson equation to study the mechanisms of channel formation and of current flow through the device. The conduction band profile for the AlInN/InN HFET using self consistent solution of the Schrödinger and Poisson equation over the entire device structure is shown in Fig. 4.1. The band profile is calculated for the first two sub band energy (i.e, for E_1 and E_2 quantum states) for In mole fraction of 0.1 and 0.05 as higher order band energy is negligible effect. The x denotes the distance away from the surface to the inside of the HFET structure. While those using an oxide layer beneath the gate, the conduction band profile obtained for In content of 0.1 is shown in Fig.4.2. A large conduction band discontinuity results in better electron confinement and allows for a higher sheet charge density in the well at the Hetero interface [23]. A large conduction band offset of about 2.7eV and 3.08 eV for In mole fraction of 0.1 and 0.05 is obtained for the proposed device, which ensure the better confinement and higher sheet charge density.

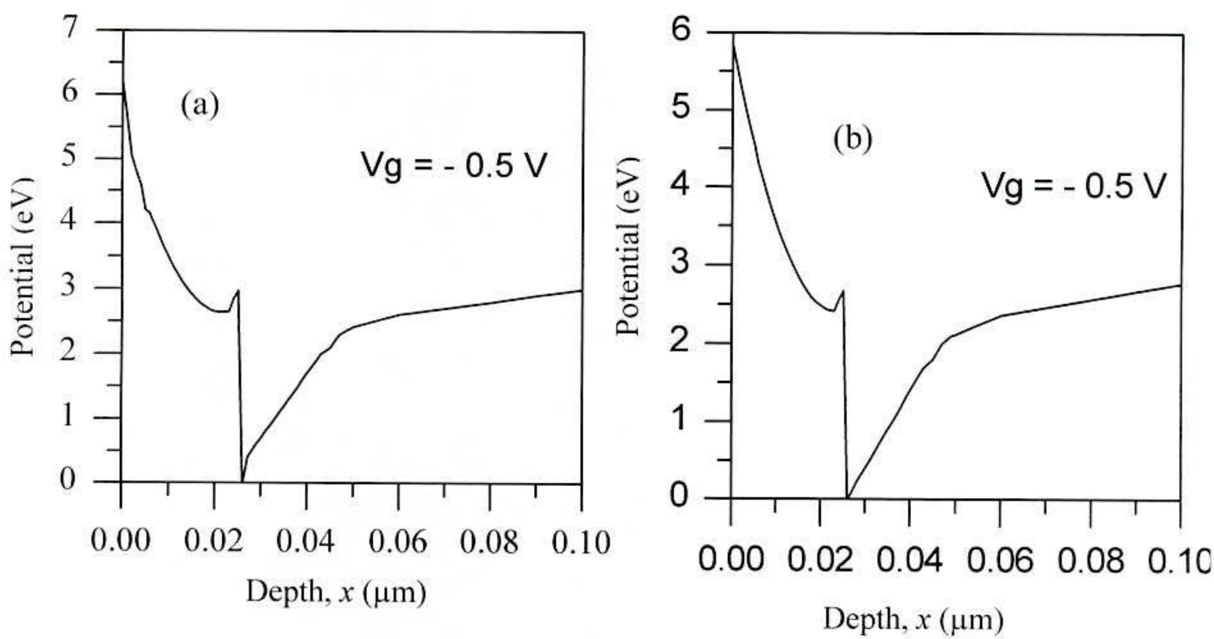

Figure 4.1 Simulated conduction band profile as a function of distance for (a) $m = 0.05$ and (b) $m = 0.1$ of AlInN/InN HFET

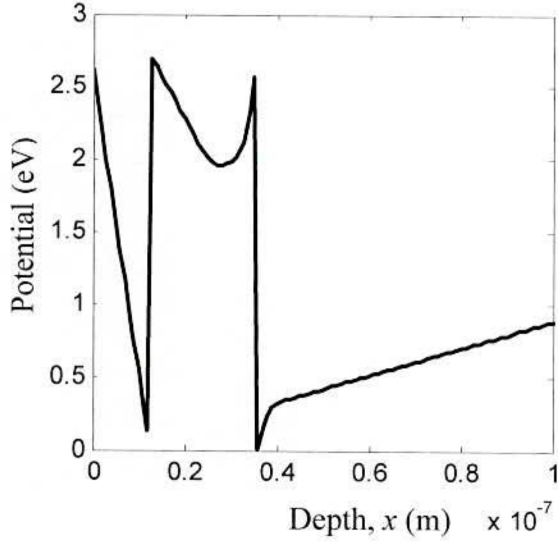

Figure 4.2: Simulated conduction band profile as a function of distance for $m = 0.1$ and Vg = - 0.5 V of AlInN/InN MOSHFET

4.2.2 Position dependent charge distribution

The distribution of the free charge in the channel of AlInN/InN HFET is shown in Fig. 4.3 for In content of 0.1 and 0.05, respectively. The calculations here shown have been obtained considering the polarization charge at the AlInN/InN interface. As long as the 2DEG concentrations are very high ($\sim 10^{20}$ cm^{-3}), the influence of the background concentration of free carrier is neglected. As shown in Fig.4.3 when the In content of m = 0.05 and 0.01, the 2DEG forms at the hetero interface with a peak concentration of high up to 4.73×10^{20} and 4.5×10^{20} cm^{-3}, respectively. The 2DEG sheet density is calculated to be as high as 0.94×10^{14} and 0.89×10^{14} cm^{-2}, respectively. While those using an oxide layer beneath the gate the peak concentration changes to be 6.2×10^{20} and 5.9×10^{20} cm^{-3}, respectively and the 2DEG sheet density is calculated to be as high as 1.85×10^{14} and 1.66×10^{14} cm^{-2}, respectively. The high density carrier mainly caused by two factor, one is the large piezoelectric polarization caused by the significant lattice mismatch between AlInN and InN. The other is strong quantum confinement effect caused by the large conduction band offset of about 2.7eV and 3.08 eV for In mole fraction of 0.1 and 0.05. The sheet carrier density for the proposed AlInN/InN HFET is increased by almost one order of magnitude as compared to $\sim 1 \times 10^{13}$ obtained in a conventional GaN based HFET [66-68].

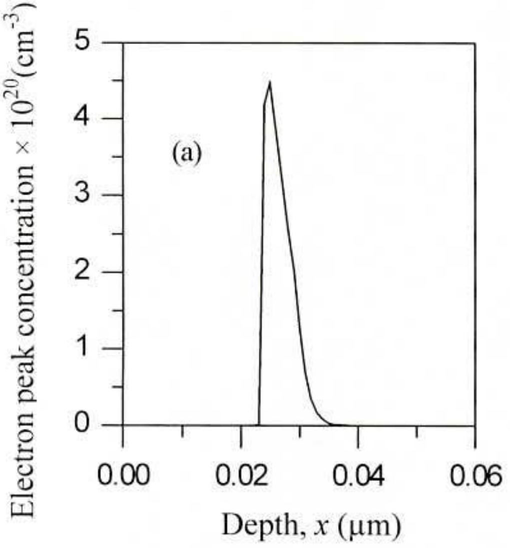

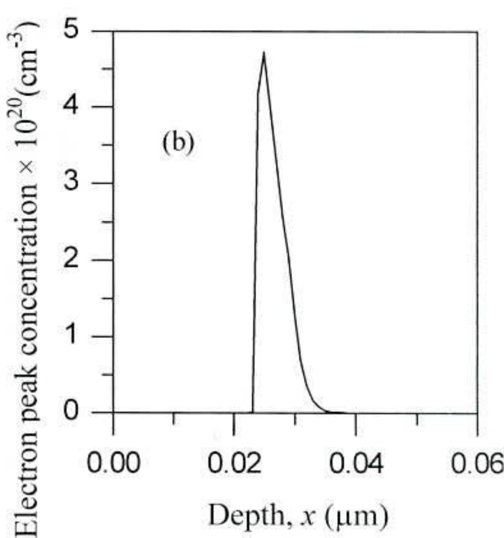

Figure 4.3: Simulated electron distribution as a function of distance for Vg = - 0.5 V and (a) m = 0.1 and (b) m = 0.05 of AlInN/InN HFET

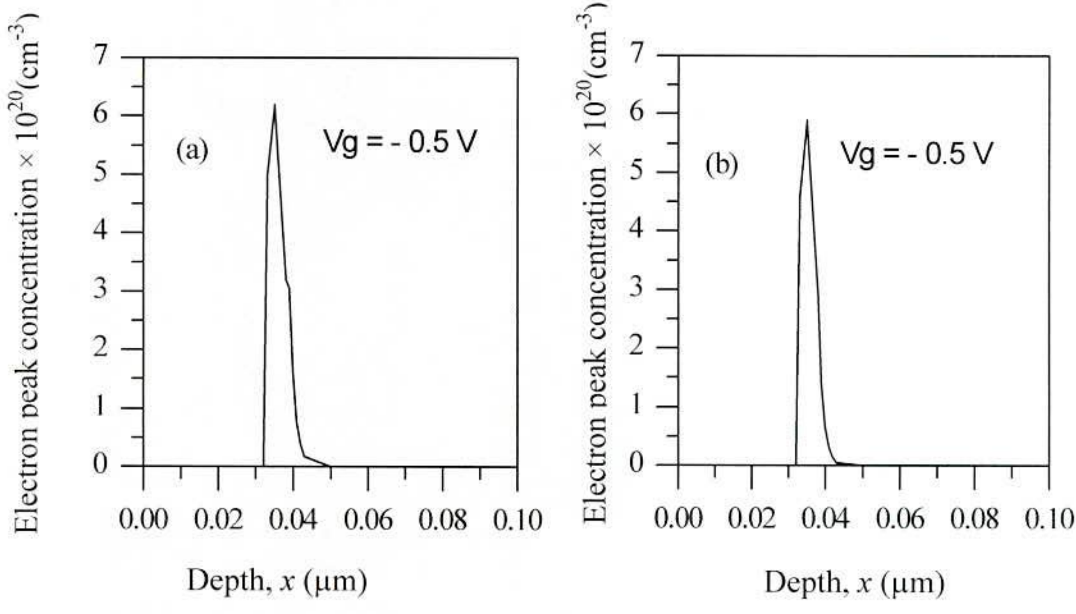

Figure 4.4: Simulated electron distribution as a function of distance for (a) $m = 0.05$ and (b) $m = 0.1$ of 0.25 μm SiO_2/AlInN/InN MOSHFET

4.2.3 Composition dependent carrier concentration

Figure 4.5 shows the electron peak concentration as a function of In mole fraction m. It can be seen that with increasing the In content, the electron peak concentration decreases. Due to sharp decrease of the piezoelectric polarization rather than the slight increase of the spontaneous polarization in AlInN layer with the In content the peak concentration is reduced. Another reason for the decrease of 2DEG is the weaker carrier confinement with the conduction band offset decreased. The value found to be for the In composition of 0.05, 0.1 and 0.15 are 4.73×10^{20}, 4.5×10^{20} and 4.3×10^{20} cm^{-3}, respectively for the AlInN/InN HFET. While those using the oxide layer these are 6.2×10^{20}, 5.9×10^{20} and 5.69×10^{20} cm^{-3}, respectively. The increase of the sheet carrier concentration by the SiO_2 top layer is attributed to the reduction of the surface states that can trap electrons or to the trapping of a positive charge at the interface with the AlInN barrier that neutralizes the fixed polarization charge. A similar increase in sheet carrier density was also reported in metal-oxide-semiconductor HFET by Marso et al. [69]. Sheet carrier density for HFET is clearly larger than conventional GaN HFETs for a particular value of aluminum mole fraction and dopant layer thickness [70-71].

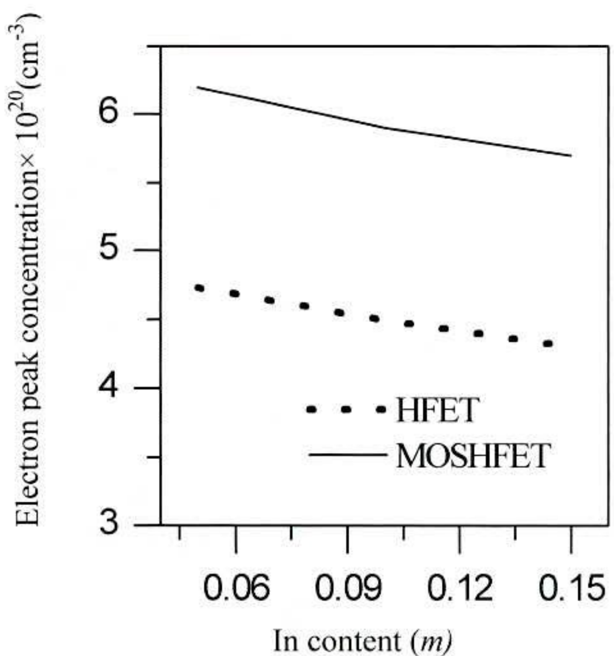

Figure 4.5: Electron peak concentration as a function of In content of AlInN/InN HFET

4.2.4 Variation of 2DEG Sheet Carrier Density with Gate to Source Voltage

An accurate charge control relation between 2DEG sheet carrier density n_s and the controlling gate voltage V_{gs} is desirable to characterize and optimize the device performance. Figure 4.6 shows the variation of sheet carrier density with gate voltage for 0.25μm gate length HFET for the different values of In content. Figure shows that, n_s increase with the increase in V_{gs} from threshold voltage due to increase in conduction band discontinuity (ΔE_c). Figure 4.7 shows the variation of sheet carrier density with gate voltage for HFET in comparison to MOSHFET structures. Though the maximum sheet carrier density increases with the introduction of oxide but a slight gate voltage swing is observed with the introduction of oxide layer. The maximum value of sheet carrier density is found to be 2.35×10^{14} cm^{-2} for HFET, while those using an oxide layer this value is 2.74×10^{14} cm^{-2} for a $V_{gs} = 0$ V with dopant layer thickness of 280 A^0. The slope of n_s–V_{gs} curve corresponds to the capacitance of the structure, which is directly related to the separation between the gate and the 2DEG, i.e., the thickness of AlInN layer. As the AlInN

layer thickness increases, the slope of n_s–V_{gs} curve beyond threshold decreases. Thus, a higher value of AlInN layer thickness is desirable to achieve high value of 2DEG density and lower values of gate capacitance [68]. However, the parallel conduction in dopant layer imposes an upper limit on AlInN layer thickness, but with the introduction of dielectric under the gate region, the slope decreases for constant value of barrier layer thickness [68].

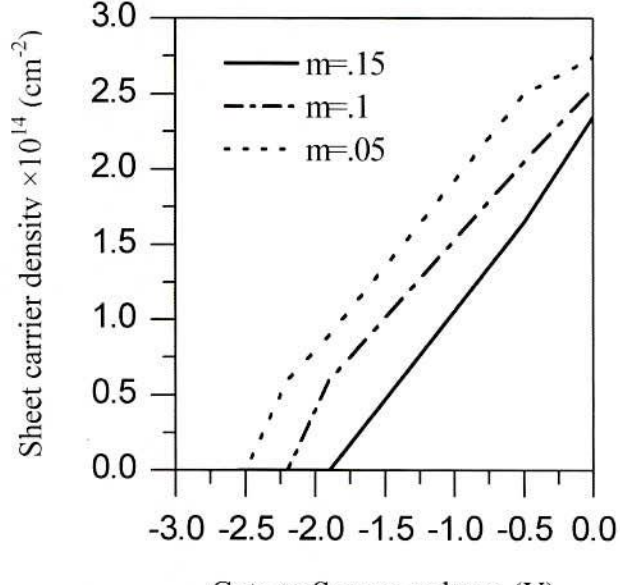

Figure 4.6: Variation of 2DEG sheet carrier density with gate source voltage for different In content

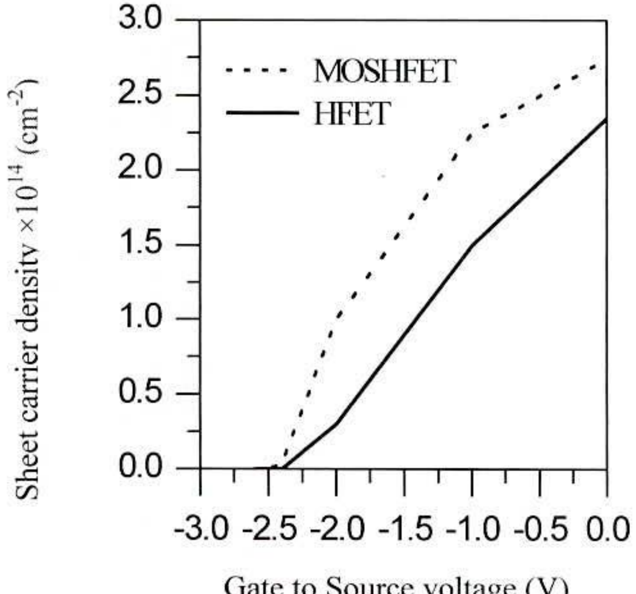

Figure 4.7: Variation of 2DEG sheet carrier density with gate source voltage for HFET and MOSHFET at m = 0.1

4.3 Scattering Mechanism

When an electron moves through a semiconductor, it suffers scattering from various scattering sources. If one considers a beam of electrons moving initially with the same momentum, then due to the scattering processes, the momentum and energy will gradually lose coherence with the initial state values. The average time takes to loss coherence of the initial state properties is called the relaxation time or scattering time. The total scattering time, τ_{sc} can be calculated as a sum of the scattering times due to each scattering process by Matthiessen's rule

$$\frac{1}{\tau_{sc}} = \sum_i \frac{1}{\tau_{sc}^{(i)}}, \tag{4.1}$$

where τ_{sc}^{i} is the scattering time of the electrons due to the individual scattering process. The scattering mechanisms have a large effect in limiting the mobility in InN-based devices. The scattering mechanisms considered are impurity scattering, dislocations scattering, interface roughness, alloy disorder scattering and phonons scattering. Impurity scatterings for 2DEG carriers can be investigated in two parts; an ionized impurity scattering due to remote donors or surface donors which is effective in modulation-doped structures and an ionized impurity scattering due to interface charges or simply background impurity scattering which is effective in all structures. Transport scattering rate due to a homogeneous background donor density of N_{back} is given by

$$\frac{1}{\tau_{back}} = N_{back} \frac{m^*}{2\pi\hbar^3 k_F^3} \left(\frac{e^2}{2\varepsilon}\right)^2 \int_0^{2k_F} dq \frac{P_0^2}{(q + q_{TF} G(q))^2} \frac{q}{\sqrt{1 - \left(\frac{q}{2k_F}\right)^2}} \tag{4.2}$$

The scattering rate due to surface donors is given by

$$\frac{1}{\tau_r} = N_s \frac{m^*}{2\pi\hbar^3 k_F^3} \left(\frac{e^2}{2\varepsilon}\right)^2 \int_0^{2k_F} dq \frac{P_0^2 e^{-2q|d|}}{(q + q_{TF} G(q))^2} \frac{q^2}{\sqrt{1 - \left(\frac{q}{2k_F}\right)^2}} \tag{4.3}$$

Alloy disorder scattering originates from the randomly varying alloy potential in the barrier. Scattering rate by alloy disorder is given by [72]

$$\frac{1}{\tau_{alloy}} = \frac{3b}{16} \frac{x(1-x)m^* \Omega_0 U_{AL}^2}{\hbar^3} \tag{4.4}$$

where x is the alloy mole fraction, Ω_0 is the volume occupied by one atom and U_{AL} is the alloy potential. The factor b is called the Fang–Howard expression [73] of wave functions for Hartree approximation of a triangular well and is given by [74]

$$b = (\frac{33e^2 m^* n_{2D}}{8\varepsilon_0 \varepsilon_s \hbar^2})^{\frac{1}{3}}.$$

Interface roughness is an important problem for semiconductor heterostructures [75]. Scattering rate by a rough interface with a root mean square roughness height, Δ and a correlation length between fluctuations, L is given by [76]

$$\frac{1}{\tau_{ir}} = \frac{\Delta^2 L^2 e^4 m^*}{2\varepsilon^2 \hbar^3} \left(\frac{1}{2} n_{2D}\right)^2 \int_0^1 du \frac{u^4 e^{-k_F^2 L^2 u^2}}{\left(u + G(u)\frac{q_{TF}}{2k_F}\right)^2 \sqrt{1-u^2}} \tag{4.5}$$

where the integral is rendered dimensionless by the substitution $u = q/2k_F$. Phonon scattering plays an important role in limiting the electron mobility in III–nitride semiconductors. The phonon scattering is calculated by considering two scattering mechanisms, including deformation potential and polar optic phonon scattering. The expression of deformation potential scattering is given by [77]

$$\frac{1}{\tau_{dp}} = \frac{3b}{16} \frac{\Xi^2 k_B m^* T}{\hbar^3 \rho u_l^2} I_{DP}(k). \tag{4.6}$$

The expression of the mobility limited by the polar optic phonon scattering is given by Ridley as [78]

$$\frac{1}{\tau_{Po}} = \frac{e^2 \omega m^* Z_0}{4\pi\varepsilon_0 \varepsilon_p \hbar^2} \left[\frac{1}{e^{\hbar\omega/k_B T} - 1}\right] \tag{4.7}$$

where,

$$\frac{1}{\varepsilon_p} = \frac{1}{\varepsilon_\infty} - \frac{1}{\varepsilon_0}.$$

Here, $\hbar\omega$ is the polar optic phonon energy, $m*$ is the effective mass for electron; ε and ε_s are the high and low frequency dielectric constants, respectively

4.3.1 Mobility analysis

Mobility's are an important parameter which referring to the usage for high frequency application of the device. Therefore, details understanding and proper inclusion of the effects of mobility in the design and analysis of high performance electronic devices are of immense importance. Figure 4.8 shows the dependence of mobility on the carrier concentration of 0.25μm AlInN/InN HFET. The highest mobility is found to be 8.1×10^{4} $cm^{2}V^{-1}sce^{-1}$ at sheet carrier concentration $n_s = 8.79\times10^{12}$ cm^{-2} at 77 K. The mobility's found to be increased with the increase of sheet carrier density but for the sheet carrier above the value of 8.79×10^{12} cm^{-2} it starts to decrease. Because that time the various scattering effects are more significant due to the collision of more carriers. The mobility is calculated by,

$$\mu = \frac{e\langle \tau_{tot} \rangle}{m_e^*} \tag{4.8}$$

where, μ = Mobility, $\langle \tau_{tot} \rangle$ = Mean scattering time calculated using Monte Carlo Simulation, e = Electron charge, m_e^* = Electron effective mass.

At low temperatures, the different scattering processes act independently; Matheissen's rule offers a simple way of combining the effect of all scatterers. The calculation was done with a dislocation density of N_{dis} = 1×10^{8} cm^{-2}, background density N_{back} = 10^{18} cm^{-3}, surface donor density $N_s = n_s$ which is required from charge control, alloy composition x = 0.1. Relevant source of scattering has been considered, and the relative effects are clearly shown in the Fig. 4.9. At low sheet densities ($n_s \leq 8.79\times10^{12}$ cm^{-2}), charged impurity scattering from background donors, surface donors and dislocations limit the mobility. Relative concentration of the particular form of charged impurity will determine the dominant scatterer. However, as is evident from the calculation, mobility at typical AlInN/InN sheet densities is limited by short range scatterers due to alloy disorder and interface roughness. In the range of 2DEG densities $n_s \geq 8.79\times10^{12}$ cm^{-2}, alloy scattering or interface roughness scattering dominate, depending on the nature of the barrier material on the channel. The calculated values of 2DEGs mobility in AlInN/InN heterostructures are in good agreement with the reported values for InN-based heterostructures [79- 80].

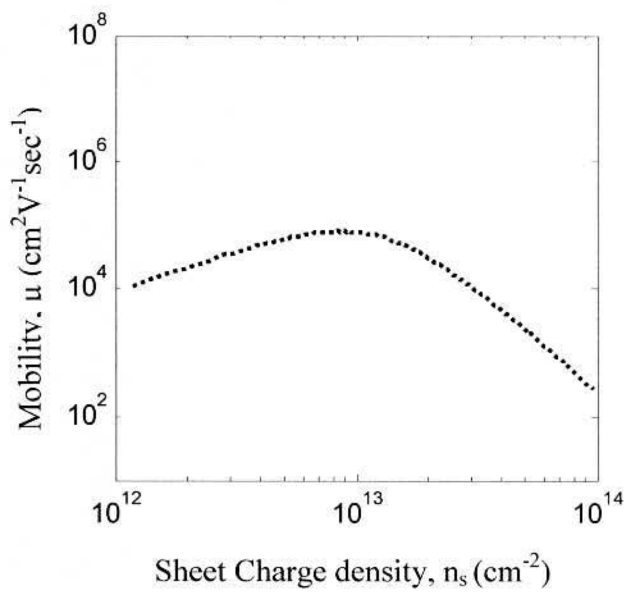

Figure 4.8: Variation of mobility with sheet charge density

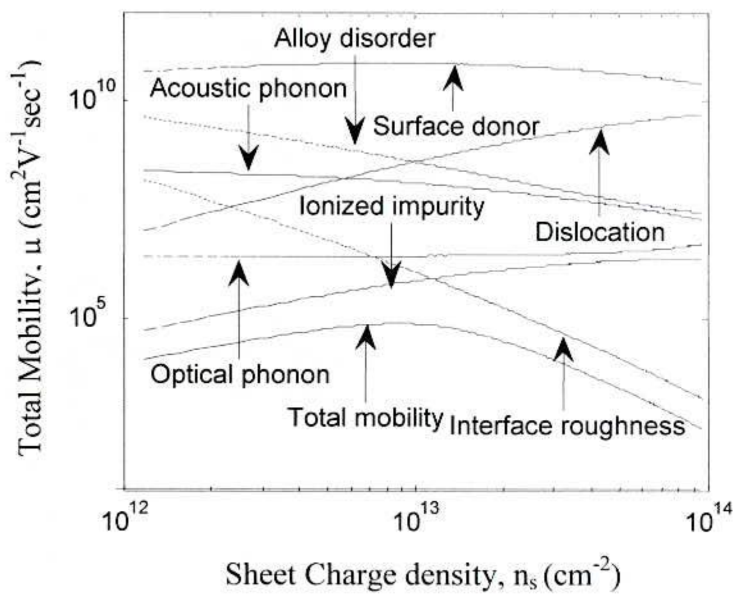

Figure 4.9: Effect of various scattering mechanism on mobility

4.3.2 Velocity field Characteristics

When an electron distribution is subjected to an electric field, the electrons tend to move in the field direction (opposite to the field *E*) and gain velocity from the field. However, because of imperfections, they scatter in random directions. A steady state is established in

which the electrons have some net drift velocity in the field direction. In most electronic devices a significant portion of the electronic transport occurs under strong electric fields. This is especially true of field effect transistors. At such high fields ($E \sim$ 1-100 kV/cm) the electrons get "hot" and acquire a high average energy. The extra energy comes due to the strong electric fields. The drift velocities are also quite high. The description of electrons at such high electric fields is quite complex and requires either numerical techniques or computer simulations. At high electric field as the carriers gain energy from the field, they suffer greater rates of scattering. The mobility thus starts to decrease. It is usual to represent the response of the carriers to the electric field by velocity – field relations. At very high fields the drift velocity becomes saturated, i.e., becomes independent of the electric field. The drift velocity for carriers in most materials saturates to a value of $\sim 10^7$ cm/s. The fact that the velocity saturates is very important in understanding current flow in semiconductor devices. The velocity-field characteristic of the proposed HFET has been calculated using Monte Carlo simulation [appendix B]. Figure 4.10 shows the calculated velocity–field characteristics of 0.25μm AlInN/InN HFET. At 77 K temperature, the peak velocity is found to be 8.3×10^7 cm/sec at the field of 66 kV/cm. It is found that the velocity is substantially higher than the traditional GaN based HFETs [81].

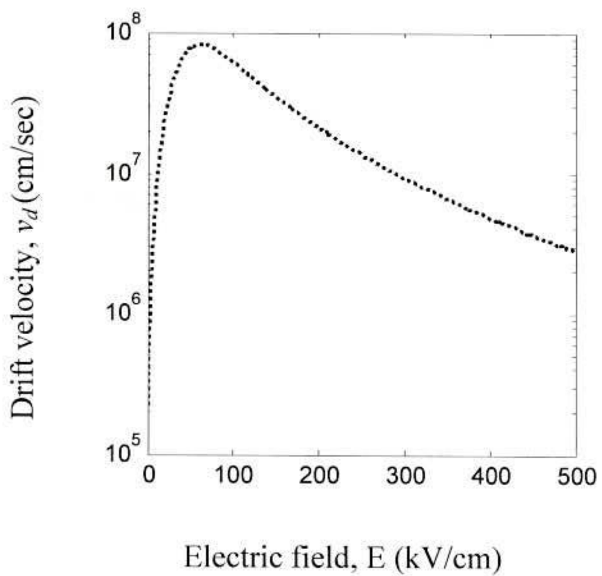

Figure 4.10: Velocity field characteristic of 0.25μm AlInN/InN HFET.

Chapter V

DC Characteristics Analysis

5.1 Introduction

The behavior of device in terms of threshold voltage, output current and transconductance is studied in this chapter. The chapter starts with a detail study of charge control parameters such as threshold voltage and I-V characteristic of the proposed device. Then, transconductance and the dependency of these parameters on gate length are also discussed.

5.2 Threshold Voltage Characteristics

The dependency of threshold (V_{th}) voltage on dopant layer thickness (d_d) for different In mole fractions of AlInN/InN HFET in comparison to MOHFET is shown Fig. 5.1. The V_{th} decreases with the increase in d_d. The negative enhancement observed in V_{th} for higher mole fractions of Al is due to the fact that higher negative voltage is required to deplete a higher density of electrons located at a larger effective distance from gate. An increase in Al mole fraction also leads to decrease in threshold voltage (V_{th}) due to corresponding increase in polarization induced sheet carrier density. This variation in sheet carrier density can be used to improve device performance for different set of geometrical parameters. As predicted, higher values of threshold voltage are observed for MOSHFETs. Because of a voltage drop at the SiO_2 gate oxide, the threshold voltage of the MOSHFET shifts to - 2.51 from -2.50 for m = 0.05 and-2.18 V to -2.19 V for m = 0.1 at 13 nm oxide layer thickness. This shift is apparent in the form of gate voltage swing for the MOSHFET structures. If the thickness of the oxide layer increases the negative enhancement of threshold voltage also increases as more voltage drop across the oxide layer. The dependency of threshold voltage on oxide layer is shown in Fig. 5.2.

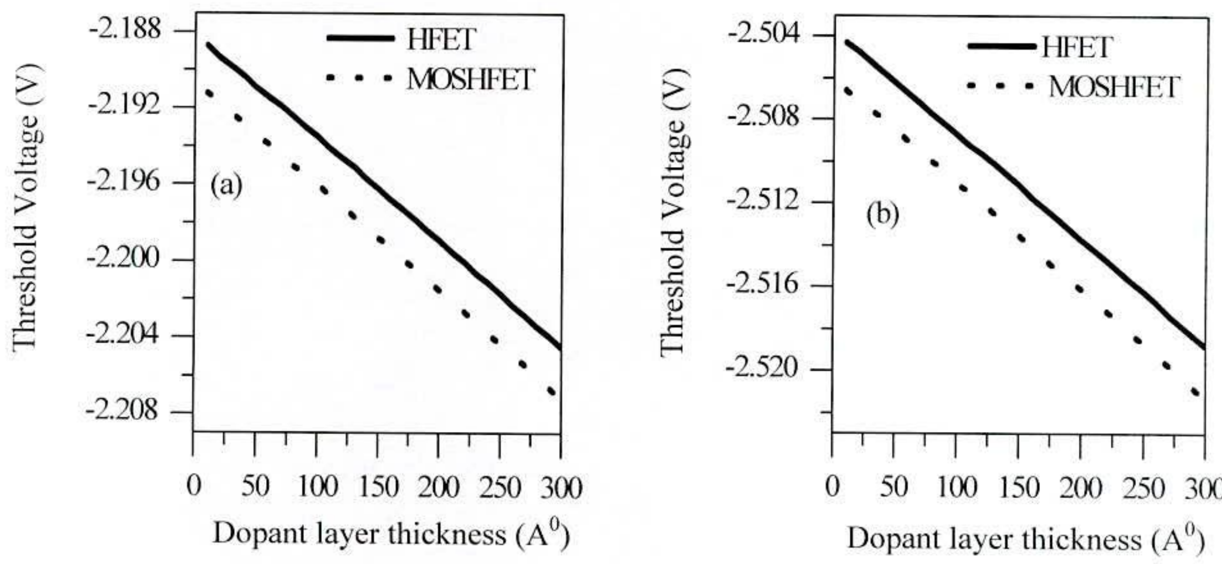

Figure 5.1: Variation of threshold voltage with dopant layer thickness for MOSHFET and HFET for (a) m = 0.1 and (b) m = 0.05

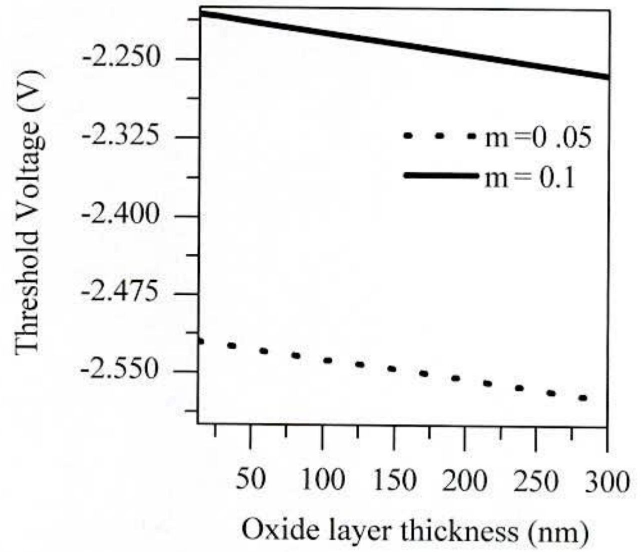

Figure 5.2: Variation of threshold voltage with oxide layer thickness

5.3 I-V Characteristics

The dc output characteristic, current-voltage (I_{ds}-V_{ds}) relation is the most important parameter which represents the performance of the device. Figure 5.3 shows the I_{ds}–V_{ds}

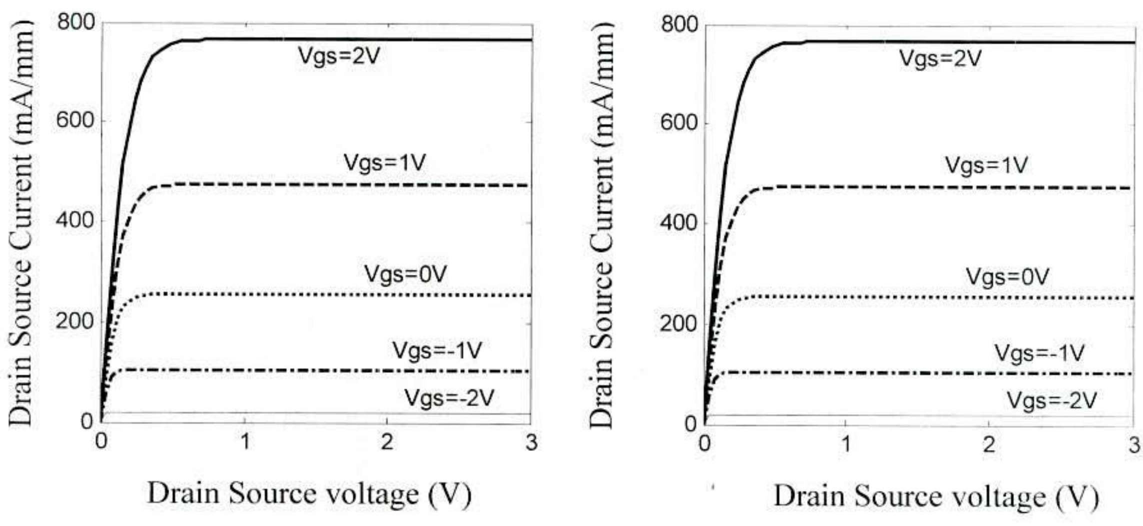

Figure 5.3: I-V Characteristics of 0.25μm AlInN/InN (a) HFET (b) MOSHFET

characteristics of 0.25 μm gate length AlInN/InN HFETs without and with oxide layer. I_{ds} increases linearly with the increase in V_{ds} in the low longitudinal field region (linear region) up to pinch off. After this value, I_{ds} doesn't vary significantly due to the velocity saturation. Drain current also increases with the increase in V_{gs} because with increase in gate to source voltage the sheet carrier concentration increases. Maximum drain current is found to be 715 and 786mA/mm for HFET and MOSHFET, respectively at V_{gs} = 2V for different values of drain source voltage. It is clear from the Fig. 5.4 that for the same values of gate and drain bias, the drain current is higher for MOSHFETs than the HFETs. The MOSHFETs show remarkable 10% increase in drain saturation current. The major cause for this rise is due to the increase in channel carrier density, which is modified by the surface states. [82]. A similar increase in peak drain saturation current was also reported in metal-oxide-semiconductor HFET by Hu et al. [83].

5.4 Saturation Drain Current Characteristics

The variation of drain current with gate bias is depicted in Fig. 5.5 for 0.25 μm AlInN/InN HFET and MOSHFET. As the gate to source voltage is increased from the threshold voltage (V_{th}), the depth of potential well at heterointerface increases, resulting in higher sheet carrier concentration and higher drain current. The dc saturation drain current, which

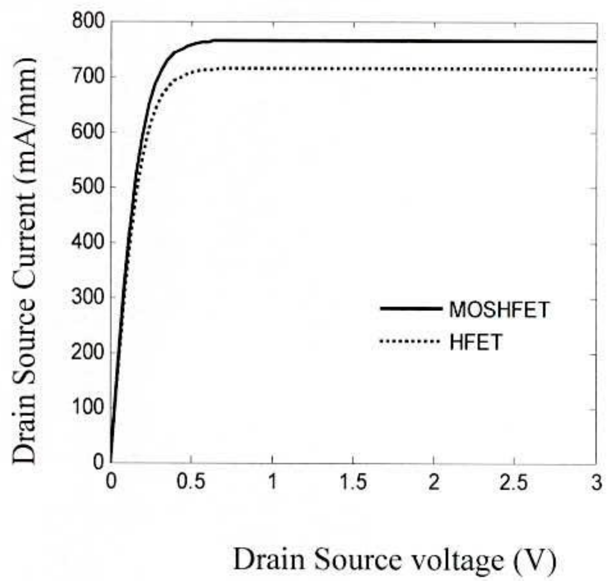

Figure 5.4: I-V Characteristics of 0.25µm AlInN/InN HFET in comparison to MOSHFET at Vg = 2V

is a key parameter for controlling maximum output RF power, is larger in MOSHFETs than in HFETs. In devices with long gate, the drain saturation current depends on electron mobility, but in short gate length devices, the electron velocity under the gate saturates, which limits the maximum current. The forward gate current, which increases exponentially as a function of gate bias, plays significant role in limiting the channel current at high positive gate biases in HFETs. To limit the gate leakage current, HFET generally operate at gate voltages ranging between threshold voltage and values slightly above zero, but the MOSHFET structures do not have the gate current limitation as is clearly shown by substantially larger values of I_{dsat}. A value of I_{dsat} = 780 and 700 mA/mm at V_{gs} = 2 V is obtained from 0.25 µm gate MOSHFET and HFET, which makes them extremely attractive for microwave applications.

5.5 Gate Length Dependent Drain Current

Figure 5.6 shows the variation of drain current with gate length for 0.25 µm HFET and MOSHFET. Drain current is found to be varied from 785 to 205 and 715 to 190mA/mm, respectively for MOSHFET and HFET with the variation of gate length from 0.25 to 1.5µm. Drain current decreases with the increase of gate length due to increase in channel resistance.

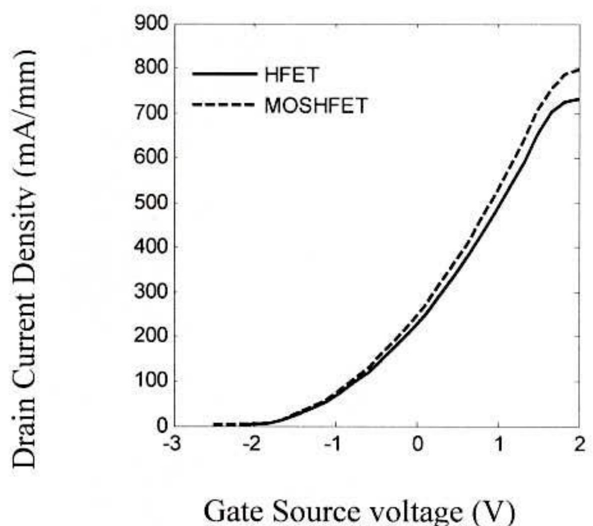

Figure 5.5: Variation of drain current with gate to source voltage

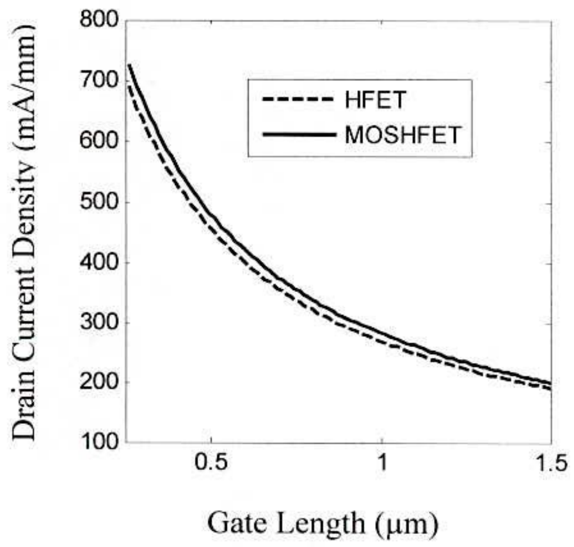

Figure 5.6: Dependence of drain current on gate length
at $V_{gs} = 2$ V, $W = 100$ μm and $m = 0.1$.

5.6 Transconductance Variation with Gate to source Voltage

The dc transfer characteristic, transconductance of a device is one of the most important indicators of device quality for microwave and millimeter wave application. Figure 5.7 shows transconductance (g_m) as a function of gate to source voltage (V_{gs}) for different

drain to source voltage (V_{ds}) at $L_g = 0.25\mu m$. The g_m increases with the increases in V_{gs} and after reaching maximum value it starts to decrease. The peak g_m occurs at the V_{gs} that just begin to cause some noticeable occupations of ionized donors under the gate. The peak value of g_m is found to be 280 and 225 mS/mm, respectively at $V_{ds} = 2V$ for HFET and MOSHFET, which is higher than the reported value for AlGaN/GaN HFET [36, 68]. High value of g_m has been attributed to high saturation velocities and high sheet carrier density. The decrease in transconductance that occurs for $V_{gs} > 1.5V$ is a characteristic feature of HFETs [84]. The MOSHFET have lower transconductance in comparison to HFET. This decrease is consistent with a larger separation between the MOSHFET channel and gate contact. Although the MOSHFET have lower transconductance in comparison to HFET, they have almost constant variation of transconductance for wide range of gate source voltages, which makes it useful for high performance amplifications.

5.7 Gate Length Dependent Transconductance

Figure 5.8 shows the dependence of transconductance on the gate length (L_g) for HFET and MOSHFET. The g_m decreases with increasing the gate length due to increase in

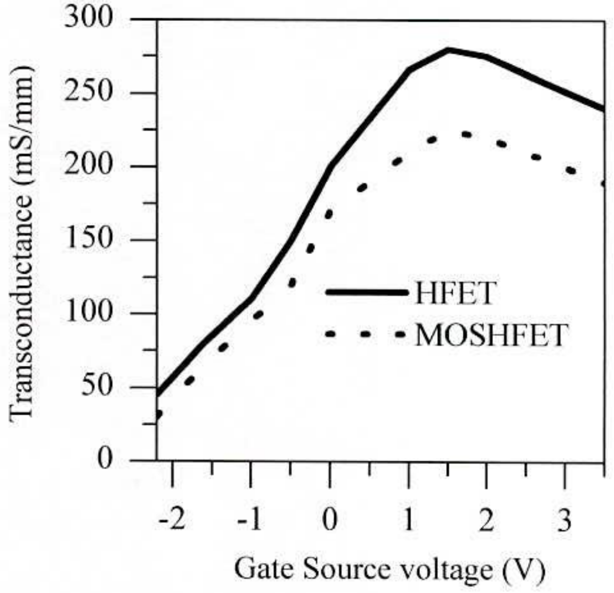

Figure 5.7: Transconductance as a function of gate to source voltage at $L_g = 0.25$ μm and $W = 100$ μm.

channel resistance which restricts the g_m. The calculated value of g_m is found to be varied from 280 to 205mS/mm and 225 to 105 mS/mm with the variation of L_g from 0.25 to 1.5μm at V_{ds} = 2 and V_{gs} = 1.5V.

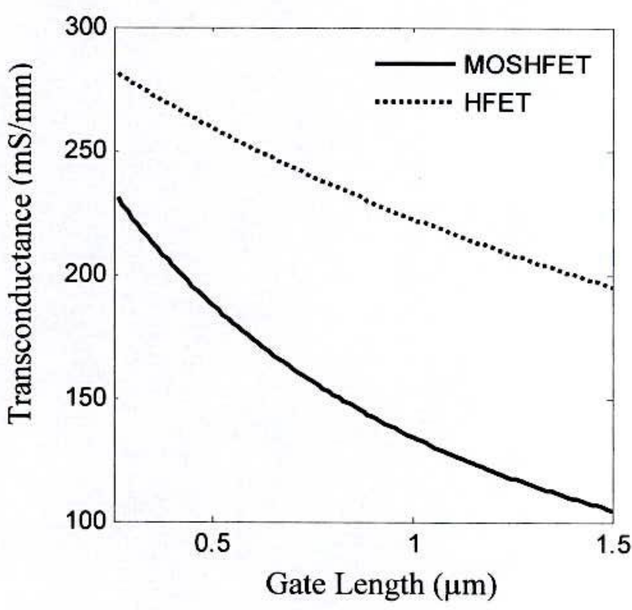

Figure 5.8: Variation of Transconductance with gate length

Khulna University of Engineering & Technology
KUET
Bangladesh
Central Library

Chapter VI

High Frequency Performance Analyses

6.1 Introduction

The microwave analog circuits for mobile communication system, optical communication system, high speed digital circuit applications and more sophisticated high speed applications require semiconductor devices with very high switching speed. Cut-off frequency which ultimately determines the switching speed of a device plays most significant role to specify the high frequency performance of HFETs. To explain the high frequency performance of the InN-based HFET, the effect of gate to source voltage and drain to source voltage on cut-off frequency is discussed. The effect of gate length which is the most important structural parameter to determine cut-off frequency is also analyzed to evaluate the high frequency performance.

6.2 Variation of Cut off Frequency with gate to source voltage

The cut-off frequency (f_t) is an important figure of merit for microwave field effect transistors. The variation of cut-off frequency with gate to source voltage (V_{gs}) for AlInN/InN HFET and MOSHFET is shown in Fig. 6.1. The trend of gate to source voltage dependence cut-off frequency is similar to g_m-V_{gs} curve. The f_t increases with the increase in V_{gs} and reaches to a peak value as the sheet carrier concentration increases up to the equilibrium value, after that it begins to decrease. The maximum value of cut-off frequency (f_t) is found to be 110 and 83 GHz at V_{ds} = 2 and 1V, respectively for HFET. While those using an oxide layer beneath the gate these are 154 and 116GHz. Now, the velocity-saturated carriers, moving in a high-field region, are affected by various scattering mechanisms, thereby, decreasing the f_t. The f_t also increases with the increase in V_{ds} because with the increase in V_{ds}, the transconductance increases as the parasitic resistances are lower at higher drain to source

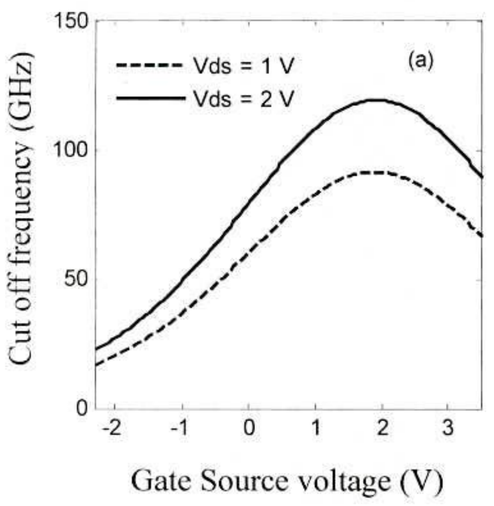

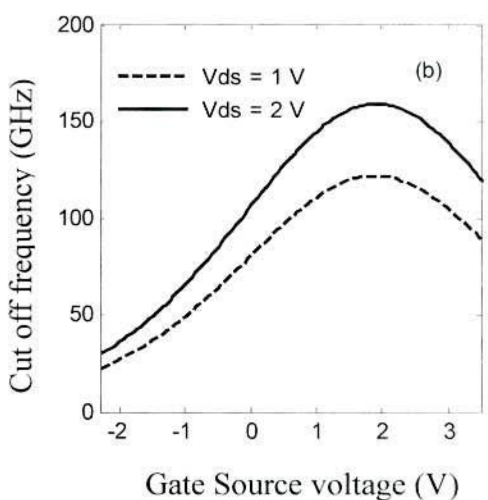

Figure 6.1: Dependency of cut off frequency as a function of gate source voltage for (a) HFET (b) MOSHFET

voltage [85]. A slightly higher cut-off frequency is observed in case of MOSHFET as shown in Fig. 6.1(b). This increase in cut-off frequency is attributed to decrease in overall capacitance of the device. The variation of cut-off frequency with gate source voltage (V_{gs}) of HFET in comparison to AlInN/InN MOSHFET is shown Fig. 6.2. The calculated values of f_t for the proposed AlInN/InN HFET and MOSHFET are found to be much higher than the reported values of AlGaN/GaN HFET and MOSHFET [36, 68, 71].

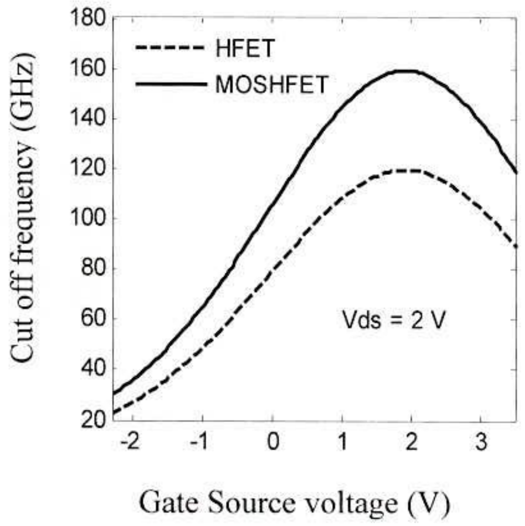

Figure 6.2: Variation of cut off frequency with gate source voltage of HFET in comparison to MOSHFET

6.3 Gate Length Dependent Cut off Frequency

The variation of cut-off frequency with gate length (L_g) for AlInN/InN HFET and MOSHFET is shown in fig. 6.3. The f_t falls sharply with increasing the L_g due to increase in electron transit time through the channel, resulting in the reduction of the cut-off frequency. The higher L_g increases the channel resistance and gate capacitance that restrict high frequency performance. The f_t varies from 110 to 12 GHz and 154 to 26GHz for HFET and MOSHFET, respectively with the variation of L_g from 0.25 μm to 1.5 μm at V_{ds} = 2 V and V_{gs} = 1.5 V.

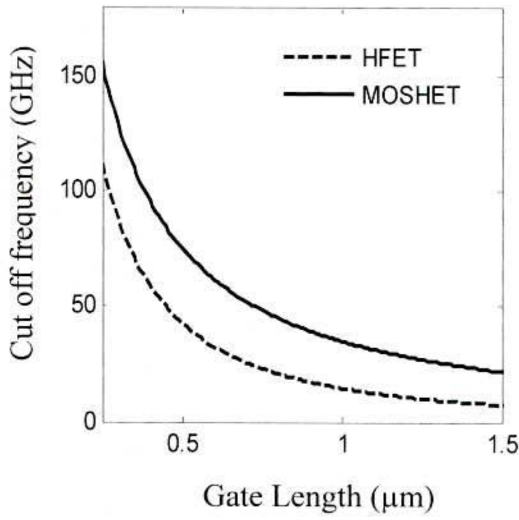

Figure 6.3: Dependency of cut off frequency on gate length

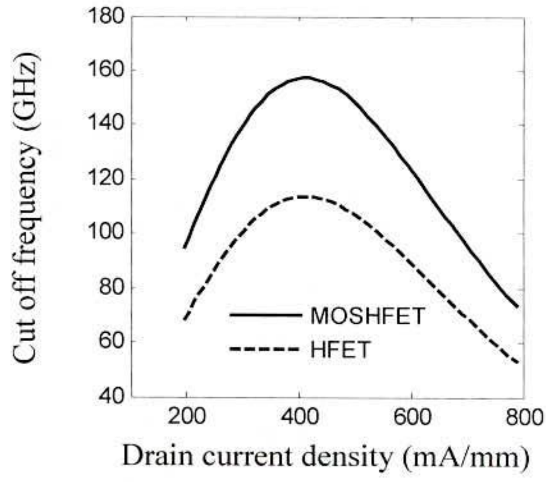

Figure 6.4: Variation of cut off frequency with drain current

6.4 Cut off Frequency and Drain Current Relation

The dependency of cut-off frequency (f_t) on drain current (I_{ds}) is shown in Fig. 6.3. A large variation of f_t has been observed with the variation in drain current. When drain current is low transconductance is low, hence low value of f_t is observed. Transconductance increases with the increase in drain current, which results in an increase in f_t. After reaching a peak, the g_m falls resulting in a fall in f_t. The peak value of f_t is found to be 110 and 154 GHz respectively for drain current of 360 mA/mm at V_{ds} = 2 V and V_{gs} = 1.5V for HFET and MOSHFET.

Chapter VII

Conclusions and Recommendations

7.1 Conclusions

InN has attracted much attention to semiconductor research communities as a very promising candidate for designing heterojunction field effect transistor (HFET) for high frequency applications. However, the practical applications of InN-based electronic devices are still immature. This dissertation has focused on the theoretical design and performance evaluation of InN based HFET without and with an oxide layer beneath the gate. A quantum mechanical charge control model of AlInN/InN HFET using the self-consistent solution of Schrödinger-Poisson equations is developed in this work. To characterize the dc and microwave performance a nonlinear analytical model is also presented. The model developed is employed to study the impact of device performance on various parameters.

Sheet carrier concentration is the key parameter to understand the HFET operation. By solving Schrödinger-Poisson equations self consistently the 2DEG distributions and sheet densities in AlInN/InN heterostructure field effect transistor are calculated. Owing to the large band offset and strong polarization effect an extremely high 2DEG sheet density of 0.94×10^{14} and 0.89×10^{14} cm^{-2} is observed with In content of m = 0.05 and m = 0.1, respectively. Examination of dependency of the electron peak concentration on the In content shows that the extremely high density 2DEG is mainly due to the polarization effect and quantum confinement effect which are highly enhanced by decreasing the In content in the $Al_mIn_{1-m}N$ barrier. The value of peak concentration found to be 4.73×10^{20} and 4.5×10^{20} cm^{-3}, respectively for the AlInN/InN HFET at m = 0.05 and 0.1. While those using an oxide layer beneath the gate the peak concentration changes to be 6.2×10^{20} and 5.9×10^{20} cm^{-3}, respectively. It is very important to know how sheet carrier density (n_s)

varies with gate to source voltage. The value of n_s increases with the increase in V_{gs} from threshold voltage due to increase in conduction band discontinuity (ΔE_c). Varying the gate to source voltage from -2.6 to 0 V, the peak value of n_s was found to be 2.35×10^{14} cm^{-2} for HFET, while those using an oxide layer this value was 2.74×10^{14} cm^{-2}. The large values of n_s are attributed to the presence of polarization induced charges in AlInN/InN HFETs. The sheet carrier densities obtained are one order higher than the conventional GaN-based devices [68].

The carrier mobility is another very important issue for device performance. The highest mobility for the HFET is found to be 8.1×10^4 $cm^2V^{-1}sce^{-1}$ at $n_s = 8.79\times10^{12}$ cm^{-2} at 77 K. The peak velocity of the carrier for the proposed device is found to be 8.3×10^7 cm/sec at the field of 66kV/cm. It is found that the velocity is substantially higher than the conventional GaN based HFETs [71]. At low sheet densities ($n_s \leq 8.79\times10^{12}$ cm^{-2}), charged impurity scattering from background donors, surface donors and dislocations limits the mobility. Relative concentration of the particular form of charged impurity determines the dominant scatterer. However, as is evident from the calculation, mobility at typical AlInN/InN sheet densities is limited by short range scatterers due to alloy disorder and interface roughness.

The DC characteristic which represents the performance of the device includes mainly drain current and transconductance. A clear gate controlled current-voltage characteristic is observed. The peak current density was found to be 715 and 786mA/mm for HFET and MOSHFET, respectively at V_{gs} of 2 V for different values of drain source voltage. The drain current was found to be higher for the MOSHFETs in comparison to HFET. With the variation of gate length (L_g) from 0.25 to 1.5 μm drain current varies from 786 to 205 mA/mm and 715 to 180 mA/mm, respectively for MOSHFET and HFET. The peak value of transconductance (g_m) was found to be 280 and 225 mS/mm for HFET and MOSHFET, respectively at V_{ds} of 2V, which is higher than the reported value for GaN HFET and MOSHFET [36, 68]. The g_m varies from 280 to 205 mS/mm and 225 to 105 mS/mm with the variation of L_g from 0.25 to 1.5 μm at V_{ds} of 2 V and V_{gs} of 1.5 V. High value of g_m has been attributed to high saturation velocities and high sheet carrier density.

The cut-off frequency (f_t) is an important figure of merit that describes the use of device in microwave applications. The maximum value of cut-off frequency (f_t) is found to be 110 and 83 GHz at V_{ds} of 2 and 1V, respectively for HFET. While those using an oxide layer beneath the gate these values were 154 and 116 GHz. The f_t was varied from 110 to 12 GHz and 154 to 26 GHz for HFET and MOSHFET, respectively with the variation of L_g from 0.25 μm to 1.5 μm at V_{ds} of 2 V and V_{gs} of 1.5 V. The calculated values of f_t for the proposed device are found to be much higher than the reported values of GaN-based devices [36, 70].

The above studies indicate that the proposed InN-based HFET is very promising for the fabrication of high performance high speed devices.

7.2 Recommendations

The research work described in this thesis concerned with the theoretical design of InN-based HFET. The proposed HFET has been successfully designed with some exciting results. These have created the way for future work with a goal to fabricate practical InN-based high performance HFET. But still there are many areas where further work is required. The works remaining for future study are discussed as follows.

The maximum power output is not calculated in this work. It is required to determine the maximum power output of the device in future work which is very important device performance parameter at high frequencies.

The high frequency performance is hampered by noise generated inside the device. More works are needed to determine the noise figure so that the analysis of high frequency performance becomes more accurate.

In this work, the drain current for different biases are determined which is very exciting but the breakdown voltage is not determined which a crucial limiting parameter of device performance.

The simulation has been done for this thesis by one dimensional Schrodinger- Poisson's equation. More accurate results can be obtained further solving two or three dimensional Schrodinger- Poisson's equation and also the drain current and other parameters can be calculated directly.

I_d-V_{ds} should be calculated using Monte Carlo Simulation and compared to the analytically calculated I_d-V_{ds}

Further work can be extended to determine the breakdown voltage. InN-based HFET is designed with self aligned gate, but there is an option to determine the performance for T gate which is treated as more advanced technology now-a-days.

REFERENCES

1 M. S. Shur, R. Gaska, M. Asif Khan and G. Simin, "Wide Band GapElectronic Devices", IEEE International Caracas Conference on Devices, Circuits and Systems, pp. 1-8, 2002.

2 C.A. Mead, "Schottky barrier gate field effect transistor," Proc. IEEE, Vol. 59, 1966, p. 307-308.

3 K. Shoinohara, Y. Yamashita, A. Endoh, et al., IEEE Electron Device Lett. 22, 507 2001).

4 Beatriz G. Vasallo,Nicolas Wichmann,Sylvain Bollaert, et al., IEEE Trans. on Electron Devices 54, 2815 (2007)

5 Toshihide IDE, Mitsuaki Shimizu, et al., Jap. J. of Appl. Phys. 46, 2334 (2007).

6 Takashi Mimura, Jpn. J. Appl. Phys. 44, 8263 (2005).

7 V. M. Polyakova and F. Schwierz, J. Appl. Phys. 101, 033703 (2007).

8 E. Bellotti, B. K. Doshi, K. F. Brennan, J. D. Albrecht, and P. P. Ruden, "Ensemble Monte Carlo study of electron transport in wurtzite InN", J. Appl. Phys., Vol. 85, no. 2, p. 916, February 1999.

9 K. T. Tsen, C. Poweleit, D. K. Ferry, H. Lu and W. J.Schaff, Appl. Phys.Lett. **86**,222103, 2005

10 B. E. Foutz, S. K. O'Leary,M.S. Shur and L.F. Eastman,J. Appl Phys., Vol .85, pp.7727, 1999

11 Ashraful G. Bhuiyan, , "ArF Excimer Laser-Assisted Metalorganic Vapor-Phase Epitaxy: A New Approach for Indium Nitride (InN) Semiconductor Growth University of Fukui,Japan, PhD Dissertation, March 2004

12 C. L. Wu, C.-H. Shen, H.-W. Lin, H.-M. Lee, and S. Gwo,Appl. Phys.Lett., vol. 87, p. 241916, 2005

13 C.-L. Wu, C.-H. Shen, and S. Gwo, Appl. Phys. Lett. **88**,032105, 2006

14 Y. C. Kong, Y. D. Zheng, C. H. Zhou, Y. Z. Deng, et al., Solid-State Electronics 49, 199 (2005).

15 O. Ambacher, J. Smart, J.R. Shealy, N.G. Weimann, K. Chu, M. Murphy, W.J. Schaff, L.F. Eastman, R. Dimitrov, L. Wittmer, M. Stutzmann, W. Rieger, and J. Hilsenbeck, Two dimensional electron gas induced by spontaneous and

piezoelectric polarization charges in N- and Ga-face AlGaN/GaN heterostructures, J Appl Phys 85 (1999), 3222-3233.

16 Rashmi, A. Agrawal, S. Sen, S. Haldar, and R.S. Gupta, 2-D analytical model for current–voltage characteristics and output conductance of AlGaN/GaN MODFET, Microwave Opt Technol Lett. 27 (2000), 413-419.

17 K Kubota, Y Kobayshi, K. Fujimoto, J.Appl. Phys. **66**, pp. 2984, 1989

18 S. Keller, I. Ben Yaacob, S. P Denverse, U K Mishra, Proceedins of the International Workshop on Nitride Semiconductors (IWN 2000),Nagoya, Japan, IPAP conference siries 1,p.233 (2000)

19 W. J. Schaff , H. Lu, J. Hwang, H. Wu, Proceedins of the seventh biennial IEEE/Cornell Conference on Advance concept in High Performance Devices",Agust 7-9,pp 2225-231,2000

20 H. Lu , W. J. Schaff, L.F. Eastman, C. Wood, Mater. Res. Soc. Symp. Proc. 693,9(2000)

21 Md. Tanvir Hasan, "InN-Based High Electron Mobility Transistors (HEMTs)", Msc Dissertation, Kuet, December 2007

22 Masaaki Kuzuhara, "Device Technology Based on New III-N Heterostructures", CS Mantech Conference, May 18th-21st, 2009, Tampa, Florida, USA

23 Md. Tanvir Hasan, Ashraful G. Bhuiyan, and Akio Yamamoto, Solid-State Electronics 52, 134 (2008).

24 Md. Tanvir Hasan and Ashraful G. Bhuiyan, submitted to J. Appl. Phys.

25 Y. C. Kong, Y. D. Zheng, C. H. Zhou, Y. Z. Deng, et al., Solid-State Electronics 49, 199 (2005).

26 K. Kodama and M. Kuzuhara, IEICE Electronics Express vol.5, pp.1074-1079 (2008).

27 Y. Ohno and M. Kuzuhara, IEEE Trans. Electron Devices, vol.48, pp.517-523 (2001).

28 D. Delagebeaudeuf and N.T. Linh, Metal-(n) AlGaAs/GaAs two dimensional electron gas FET, IEEE Trans Electron Devices 29 (1982),955-960.

29 T.J. Drummond, H. Morkoc, K. Lee, and M.S. Shur, Model for modulation doped field effect transistor, IEEE Trans Electron Device Lett 3 (1982), 338-341.

30 S. Kola, J.M. Golio, and G.N. Maracas, An analytical expression for Fermi level versus sheet carrier concentration for HEMT modeling, IEEE Trans Electron Device Lett.9 (1988), 136-138.

31 A.-J. Shey and W.H. Ku, On the charge control of the two-dimensional electron gas for analytical modeling of HEMTs, IEEE Trans Electron Device Lett 9 (1988), 624-626.

32 F. Sacconi, A.D. Carlo, P. Lugli, and H. Markoc, Spontaneous and piezoelectric polarization effects on the output characteristics of AlGaN/GaN heterojunction modulation doped FETs, IEEE Trans Electron Devices 48 (2001), 450-457.

33 N. Maeda, T. Saitoh, K. Tsubaki, T. Nishida, and N. Kobayashi,Superior pinch-off characteristics at 400°C in AlGaN/GaN heterostructure field effect transistors, Jpn J Appl Phys 38 (9A/B) (1999), L987–L989.

34. M.A. Khan, J.N. Kuznia, A.R. Bhattarai, and D.P. Olson, Mater Res Soc Symp Proc 281 (1993), 769.

35 S.C. Binari, L.B. Rowland, G. Kelner, W. Kruppa, H.B. Dietrich, K.Doverspike, and D.K. Gaskill, DC, microwave, and high-temperature characteristics of GaN FET structures, In: H. Goronkin (Ed.), Proceedings of the International Symposium on Compound Semiconductors, IOP, Bristol, 1995, p. 459.

36 M.A. Khan, X. Hu, G. Sumin, A. Lunev, J. Yang, R. Gaska, and M.S.Shur, AlGaN/GaN metal oxide semiconductor heterostructure field effect transistor, IEEE Trans Electron Device Lett 21(2000), 63-65.

37 H. Morkoc, "Nitride semiconductors and devices," Springer series in Materials Science,1999.

38 O. Ambacher and J. Smart and J.R. Shealy et. al., "Two-dimensional electron gases induced by spontaneous and piezoelectric polarization charges in N- and Ga-face AlGaN/GaN heterostructures," Journal of Applied Physics, Vol. 85, No. 6, 1999, pp.3222-3233.

39 F. Bernardini, and V. Fiorentini, "Spontaneous polarization in nitride semiconductors,"Physical Review B, Vol. 57, 1998.

40 F. Bernardini, V. Fiorentini, and D. Vanderbilt, "Piezoelectric polarization in nitride semiconductors," Physical Review B, Vol. 56, 1997.41 V. Fiorentini, F. Bernardini, and O. Ambacher, "Evidence for nonlinear macroscopic polarization in III-V nitride alloy heterostructures," Vol. 90, No. 7, 2002, pp. 1204-1206.

41 V. Fiorentini, F. Bernardini, and O. Ambacher, "Evidence for nonlinear acriscopic polarization in III-V nitride alloy heterostructures," Vol. 90, No. 7, 2002, pp. 1204-1206.

42 W. Lu, J.W. Yang, M. A. Khan, and I. Adesida, "Wideband AlGaN/GaN HEMTs on SiC for low noise applications," 58th Device Research Conference. Conference Digest,2000, pp. 39-40.

43 T. Ando, A. B. Fowler, and F. Stern, "Electronic properties of two-dimensional ystems,"Review of Modern Physics, Vol. 54, No. 2, 1982.44

44 J. C. Freeman, "Basic equations for the modeling of Gallium Nitride(GaN) high electron mobility transistors (HEMTs)," NASA/TM-2003-211983, Feb. 2003.

45 B. Jogai, "Free electron distribution in AlGaN/GaN heterojunction field effect transistors," Journal of Applied Physics, Vol. 91, No. 6, March 2002, pp. 3721-3729.

46 F. Sacconi, A. D. Carlo, P. Lugli, and H. Morkoc, "Spontaneous and piezoelectric polarization effects on the output characteristics of AlGaN/GaN heterojunction modulation doped FETs," IEEE Transactions on Electron Devices, Vol. 48, No. 3, 2001, pp.450-457.

47 J.P. Ibbetson, P.T. Fini, K.D. Ness, S.P. DenBaars, J.S. Speck, and U.K. Mishra,"Polarization effects, surface states and the source of electrons in AlGAN/GaN heterostructure field effect transistors," Applied Physics Letters, Vol. 77, No. 2, 2000, pp.250-252

48 William J. Schaff, Hai Lu, Jeonghyun Hwang, Hong Wu, "Growth of InN for Heterojunction Field Effect Transistor Applications by Plasma Enhanced MBE", IEEE Transactions on Electron Devices, pp.225-231,2000

49 Brian E. Foutz,Stephen K. O'Leary, Michael **S.** Shur and Lester F. Eastman,"Transient electron transport in wurtzite GaN, InN, and AlN" ,Journal of Applied Physics **85,** 11 1 June 1999

50 Brennan, K.F.; Bellotti, E.; Farahmand, M.; Haralson, J., 11; Ruden, P.P.; Albrecht, J.D.; Sutandi, **A.,** "Materials theory based modeling of wide band gap semiconductors: from basic properties to devices", , Solid-state Electron. (UK), Solid-state Electronics, ~01.44, no.2 p. 195-204

51 Bellotti, E.; Doshi, B.K.; Brennan, K.F.; Albrecht, J.D.; Ruden, P.P, "Ensemble Monte Carlo study of electron transport in wurtzite InN", Joumal of Applied Physics, vo1.85, no.2 p. 916-23, January 15, 1999.

52 R. Vetury, N.Q. Zhang, and U.K. Mishra, "The impact of surface states on the DC and RF characteristics of AlGaN/GaN HFETs," IEEE Trans. on Electron Devices, vol.48, no. 3, 2001, pp. 560-566.

53 G. Meneghesso et. al., "Surface-related drain current dispersion effects in AlGaN-GaN HEMTs," IEEE Transactions on Electron Devices, Vol. 51, No. 10, 2004, pp. 1554-1561.

54 S.C. Binari, P.B. Klein, and T.E. Kazior, "Trapping effects in GaN and SiC microwave FETs," Proceedings of the IEEE, Vol. 90, No. 6, 2002, pp. 1048-1058.

55 S.C. Binari et. al, "Trapping effects and microwave power performance in AlGaN/GaN HEMTs," IEEE Transactions on Electron Devices, Vol. 48, No.3, 2001, pp. 465-471.

56 P.B. Kelin et. al., "Effect of deep traps on sheet charge in AlGaN/GaN high electron mobility transistors," Electronics Letters, 2001.57 W. Kruppa et. al., "Low-frequency dispersion characteristics of GaN HFETs", Electronics Letters, 1995.

57 W. Kruppa et. al., "Low-frequency dispersion characteristics of GaN HFETs," Electronics Letters, 1995.

58 R.J. Trew, "SiC and GaN Transistors - Is there one winner for Microwave power applications," Proceedings of the IEEE, Vol. 90, No. 6, June 2002.

59 J. Park, M.W. Shin, and C.C. Lee, "Thermal modeling and measurement of GaN based HFET devices," IEEE Electron Device Letters, Vol. 24, No. 7, July 2003.

60 B.E. Foutz et. al., "Transient electron transport in GaN, InN, and AlN", Journal of Applied Physics, Vol. 85, No. 11, 1999.

61 H. Sazaw, K. Hirata, M. Kosaki, N. Shibata, K. Furutal, S. Yagi, Y. Tanaka, A. Kinoshita, M. Shimizu and H. Okumura, "Evaluation of AlGaN/GaN-HFET with HfAlO gate insulator", phys. stat. sol. (c) vol. 4, no. 7, pp2748– 2751, 2007.

62 D.E. Root, "Foundations of measurement based modeling for nonlinear circuit simulation," in IEEE MTT-S New Directions in Nonlinear RF and Microwave Characterization Workshop (WMFF), 1996, pp. 1-17.

63 M. Higashiwaki, N. Onojima, et al., "High f_T and f_{max} AlGaN/GaN HFETs achieved by using thin and high-Al-composition AlGaN barrier layers and Cat-CVD SiN passivation", phys. status solidi (a), vol. 203, no. 7, pp. 1851-1855, May 2006.

64 A. Endoh, Y. Yamashita, K. Ikeda, et al., "Fabrication of sub-50-nm-gate AlGaN/GaN HEMTs on sapphire", phys. status solidi (c), vol. 0, no.7, pp. 2368-2371, Dec 2003.

65 O. Ambacher and J. Majewski,C.Smart and J.R. Shealy et. al., "Pyroelectric properties of Al(In)GaN/GaN hetero and quantum well structure," Journal of Physics: Condens matter Vol. 14pp.3399-4334, 2002,

66 F. Sacconi, A. D. Carlo, P. Lugli, and H. Morkoc, "Spontaneous polarization and piezoelectric constants of III-V nitrides, Vol. 56, No. 16, pp.R100244-7,1997

67 Rashmi a, Abhinav Kranti, S. Haldar, R.S. Gupta, "An accurate charge control model for spontaneous and piezoelectric polarization dependent two-dimensional electron gas sheet charge density of lattice-mismatched AlGaN/GaN HEMTs", Solid-State Electronics, Vol. 46 (2002), pp. 621–630

68 Ruchika Aggarwal, Anju Agrawal, Mridula Gupta, andR. S. Gupta, "Analytical performance evaluation of AlGaN/GaN metal insulator semiconductor heterostructure field effect transistor and its comparison with conventional HFETs for high power microwave applications", microwave and optical technology letters, vol. 50, no. 2, February 2008

69 Michel Marso, Gero Heidelberger, Klaus Michael Indlekofer, Juraj Bernát, Alfred Fox, P. Kordoš, and Hans Lüth, "Origin of Improved RF Performance of AlGaN/GaNMOSHFETs Compared to HFETs", IEEE Transection on Electron devices, VOL. 53, NO. 7, July 2006

70 O. Ambacher and J. Smart and J.R. Shealy et. al., "Two-dimensional electron gases induced by spontaneous and piezoelectric polarization charges in undoped and doped AlGaN/GaN heterostructures," Journal of Applied Physics, Vol. 87, No. 6, 2000, pp.334-344.

71 Ruchika Aggarwal, Mridula Gupta, R. S. Gupta and Anju Agrawal., "An analytical drain current model for AlGaN/GaN metal insulator semiconductor heterostructure

field effect transistor: A comparative study with conventional HFETs for high power microwave applications", Proceedings of Asia Pacific Microwave Conference, IEEE, 2007

72 M. J. Kearney and A. I. Horrell, Semicond. Sci. Technol., Vol. 13, pp. 174, (1998).

73 F. F. Fang and W. E. Howard, Phys. Rev. Lett., Vol. 16, pp. 797, (1966).

74 J. H. Davies, "The Physics of Low-Dimensional Semiconductors", Cambridge: Cambridge University Press, (1998).

75 D. Zanato, S. Gokden, N. Balkan, B. K. Ridley and W. J. Schaff, Semicond. Sci. Technol., Vol. 19, pp. 427, (2004).

76 Debdeep Jena, Yulia Smorchkova, Chris Elsass, Arthur C. Gossard, and Umesh K. Mishra, "Electron transport and intrinsic mobility limits in two-dimensional electron gases of III-V nitride heterostructures", arXiv:cond-mat, Vol. 1, No. 0103461, (2001).

77 B. K. Ridley, B. E. Foutz and L. F. Eastman, Phys. Rev. B, Vol. 61, pp. 16862 (1999).

78 B. K. Ridley, J. Phys. C: Solid State Phys., Vol. 15, pp. 5899, (1982).

79 V. M. Polyakova and F. Schwierz, "Monte Carlo calculation of two dimensional gas mobility in InN-based heterostructures", Journal of Applied Physics, Vol. 101, , 2007, pp.033703.

80 Z. Yarar, B. Ozedmir and M. Ozedmir,"Transport and mobility properties of Bulk InN and a Two-dimensional electron gase in an InGan/InN quantum well", Journal of Electronic Materials , Vol. 36, No. 10, 2007, pp.1303-1312.

81 A. Asgari1, M. Kalafi, and L. Faraone, "Theoretical model of transport characteristics of AlGaN/GaN high electron mobility transistors", phys. stat. sol. (c) **2**, No. 3, 1047– 1055 (2005)

82 Y. Cai,a, Y. G. Zhou, K. J. Chen, and K. M. Lau, "III-nitride metal-insulator-semiconductor heterojunction field-effect transistors using sputtered AlON thin films", Journal of Applied Physics, Vol. 86, No. 6, 2005, pp.032109.

83 X. Hu, A. Koudymov, G. Simin, J. Yang, M. A. Khan, A. Tarakji, M. S.Shur, and R. Gaska, Journal of Applied Physics, Vol. 79, p-2832, 2001.

84 O. Aktas, Z.F. Fan, S.N. Mohanmmad, H. Morkoc, Appl. Phys. Lett. (1996) 3872-3874.

85 Ritesh Gupta, Abhinav Kranti, et al., "An analytical parasitic resistance dependent $I_d - V_d$ model for planar doped InAlAs/InGaAs/InP HEMT using non-linear charge control analysis", Microelectronic Engineering 60 (2002) 323–337.

APPENDIX A

The time-independent Schrodinger equation describing a particle of mass m constrained to motion in a time-independent, one-dimensional potential $V(x)$ is

$$H\psi_n(x) = \left(-\frac{h^2}{2m}\frac{d^2}{dx^2} + V(x)\right)\psi_n^2(x) = E_n\psi_n(x) \tag{1}$$

To solve this equation numerically, one must first discretize the functions. A sensible first approach samples the wave function and potential at a discrete set of $N + 1$ equally spaced points in such a way that position $x_j = j \times h_0$, the index $j = 0, 1, 2, \ldots, N$, and h_0 is the interval between adjacent sampling points. Thus, one may define $x_{j+1} \equiv x_j + h_0$. The region in which we wish to solve the Schrodinger equation is of length $L = Nh_0$. At each sampling point the wave function has value $\psi_j = \psi(x_j)$ and the potential is $V_j = V(x_j)$. The first derivative of the discretized wave function $\psi(x_j)$ in the finite difference approximation is

$$\frac{d}{dx}\psi(x_j) = \frac{\psi(x_j) - \psi(x_{j-1})}{h_0} \tag{2}$$

To find the second derivative of the discritized wave function, we use the three-point finite-difference approximation, which gives

$$\frac{d^2}{dx^2}\psi(x_j) = \frac{\psi(x_{j-1}) - 2\psi(x_j) + \psi(x_{j+1})}{h_0^2} \tag{3}$$

Substitution of Equation (3) into Equation (1) results in the

$$H\psi(x_j) = -u_j\psi(x_{j-1}) + d_j\psi(x_j) - u_{j+1}\psi(x_{j+1}) = E\psi(x_j) \tag{4}$$

where the Hamiltonian is a symmetric tri-diagonal matrix. The diagonal matrix elements are

$$d_j = \frac{\hbar^2}{mh_0^2} + v_j$$

and the adjacent off-diagonal matrix elements are

$$u_j = \frac{\hbar^2}{2mh_0^2}$$

To find the eigenenergies and eigenstates of a particle of mass m in a one-dimensional, rectangular potential well with infinite barrier energy the boundary conditions require $\psi_0(x_0) = \psi_N(x_N) = 0$. Because the boundary conditions force the wave function to zero at positions $x = 0$ and $x = L$, Equation (4) may be written as

$$(H - EI)\Psi = \begin{bmatrix} d_1 - E & -u_2 & 0 & 0 & \cdots \\ -u_2 & d_2 - E & -u_3 & 0 & \cdots \\ 0 & -u_3 & d_3 - E & -u_4 & \cdots \\ \vdots & \vdots & \vdots & \ddots & \cdots \\ \vdots & \vdots & \vdots & u_{N-1} & d_{N-1} - E \end{bmatrix} \begin{bmatrix} \Psi_1 \\ \Psi_2 \\ \Psi_3 \\ \vdots \\ \Psi_{N-1} \end{bmatrix} = 0$$

where H is the Hamiltonian matrix and I the identity matrix. The solutions to this equation may be found using conventional numerical methods. Programming languages such as MATLAB also have routines that efficiently diagonalize the tri-diagonal matrix and solve for the eigenvalues and eigenfunctions. In the preceding, we have considered the situation in which the particle is confined to one-dimensional motion in a region of length L. Outside this region, the potential is infinite and the wave function is zero. Particle motion is localized to one region of space, so only bound states can exist as solutions to the Schrodinger equation. Because the particle is not transmitted beyond the boundary positions $x = 0$ and $x = L$, this is a quantum nontransmitting boundary problem. There are, of course, other situations in which we might be interested in a region of space of length L through which particles can enter and exit via the boundaries at position $x = 0$ and $x = L$. When there are transmitting boundaries at positions $x = 0$ and $x = L$,

then $\psi_0(x_0) = 0$ and $\psi_N(x_N) = 0$. In this case there is the possibility of unbound particle states as well as sources and sinks of particle flux to consider. To deal with these and other extensions, the quantum transmitting boundary method may be used.

Appendix B

Monte Carlo Simulation of Electron Transport

The single Monte Carlo Method, as applied to calculate transport properties (mobility, velocity-field characteristics) in semiconductors, consist of a simulation of the relaxation time of one electron inside the crystal subject to applied electric field and scattering mechanisms.

The performance of semiconductor electronic devices depends on mobility of the materials in which they are fabricated. There are several methods used in the calculation of mobility, namely: variational principle (VP), iterative method (IM), relaxation time approximation (RTA), Matthiessen rule (MR) formalism, and Monte Carlo (MC) method.

The motion of the electron inside the crystal subject to electric field consists of drift and collision processes. The effect of external forces is deterministic but the collision processes affect the trajectories in a probabilistic manner. The drift process may be calculated by applying the classical laws of motion, but the collision process requires probability theory. The best way to solve this problem is using Monte Carlo method by generating uniformly distributed random numbers, and by using them to determine the time between collisions and the nature of the collisions. Flowchart of a typical Monte Carlo program is shown in Figure 3.4

Let, P is the probability that the electron is not scattered in a time interval $[t_1, t_2]$. We know that the total scattering rate per unit time is $S(k,k')$ and therefore can relate the probability $P(t)$ to the probability $P(t+dt)$.

$$P(t+dt) = P(t)\left(1 - dt\sum_{k'} S(k,k')\right) \qquad (1)$$

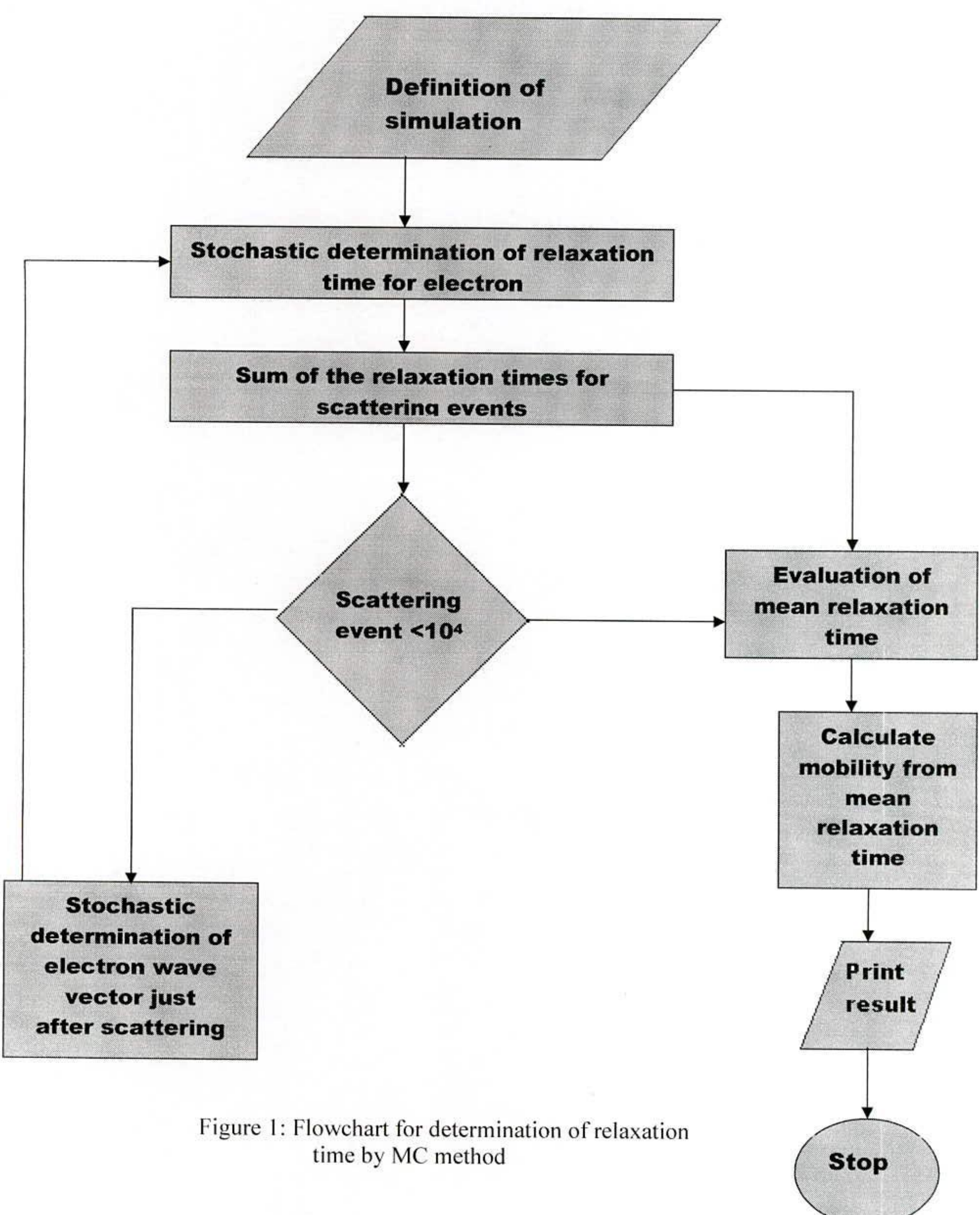

Figure 1: Flowchart for determination of relaxation time by MC method

where, $dt\sum_{k'} S(k,k')$ is the probability of an electron being scattered in the time interval dt. From the definition of differentiation, Eq. (1) is equivalent to

$$\frac{dP}{dt} = -P\sum_{k'} S(k,k') \tag{2}$$

Solving this differential equation for P in a time interval [t_1, t_2], we have

$$P = \exp\left\{-\int_1^{t_2} \sum_{k'} S(k,k')\right\} \tag{3}$$

$\sum_{k'} S(k,k')$ is generally a function of time; k can be a function of time.

We can now design the following numerical scheme to calculate the mean relaxation time for the electrons

1. At first $\tau_{tot}(k)$ for all scattering mechanisms is calculated. If these mechanisms are independent, then the probabilities for an electron being scattered add, which means that

$$\frac{1}{\tau_{tot}^{all}(k)} = \frac{1}{\tau_{tot}^{I}(k)} + \frac{1}{\tau_{tot}^{ph}(k)} + \ldots\ldots \tag{4}$$

   where the subscript *I* denotes impurity and *ph* phonon scattering.

2. The time that an electron is not scattered is determined by solving the integral Equation (3). This is accomplished in the following way: Because P is a probability; it will assume random numbers between 0 and 1. Therefore P can be replaced by such a random number r_d equi-distributed between 0 and 1, to obtain

$$r_d = \exp\left[-\int_1^{t_2} \frac{dt}{\tau_{tot}^{all}(t)}\right] \tag{5}$$

the equation now solved for t_2 (t1 is the time the electron starts)

3. Having calculated t_2, a particular electron is considered to be accelerate freely between t_1 and t_2 and then the electron is scattered to a different k' vector. Of course, we have to choose the correct k' according to the correct probability given by the dependence of $\frac{1}{\tau_{tot}}$ on k'.
4. Again a free acceleration time is calculated between period $[t_1,t_2]$ using a new r_d, and

$$r_d = \exp\left[-\int_{t_2}^{t_3}\frac{dt}{\tau_{tot}^{all}(t)}\right] \tag{6}$$

by solving Equation (5) for t3 again, the electron is considered to accelerate freely in this time period and then scatter and we continue this whole process for many scattering event, typically equal to 10^4. For these 10^4 scattering event we have found 10^4 individual relaxation time.

5. And from these relaxation times 10^4 individual mobility is calculated. From these average mobility is calculated.

Appendix C

List of the values of different parameters of InN semiconductor

Crystal structure	Wurtzite
Density (g cm **-3**)	6.81-6.89
Dielectric constant	
Static	15
high frequency	6.7-8.4
Lattice constants	a = 3.54 c = 5.70
Optical phonon energy (meV)	73
Band structure	
Energy gap (eV)	0.7
Potential deformation(eV)	7.1
Effective electron mass (in units of m_0):	0.07-0.26 ; 0.14
Effective conduction band density of states (cm^{-3})	$4.6 \times 10^{17} - 3.3 \times 10^{18}$
Ionization energy of donor	
Donor level of N vacancies V_N (meV)	40-50
Valence band	
Effective electron mass (in units of m_0)	.11

Values used for calculating strain-induced piezoelectric effects

	InN	AlN
d_{31}(cm/m)	$-1.1*10^{-10}$	$-2.0*10^{-10}$
ε (static)	15.3	8.5
C_{11} (GPa)	271	398
C_{12} (GPa)	124	140
C_{13} (GPa)	94	127
C_{33} (GPa)	200	382
α (A^0)	3.54	3.112